Regular Article

Modelling of inhomogeneous mixing of plasma species in argon–steam arc discharge for broad range of operating conditions

Jiří Jeništa[1,a], Hidemasa Takana[2], Hideya Nishiyama[2,3], Milada Bartlová[4],
Vladimír Aubrecht[4], and Anthony B. Murphy[5]

[1] Institute of Plasma Physics, AS CR, v.v.i., Plasma Chemical Technologies Department, Za Slovankou 3, 182 00 Praha 8, Czech Republic
[2] Institute of Fluid Science, Tohoku University, 2-1-1 Katahira, Aoba-ku, Sendai, Miyagi 980-8577, Japan
[3] Joining and Welding Research Institute, Osaka University, 11-1, Mihogaoka, Ibaraki, Osaka 567-0047, Japan
[4] Brno University of Technology, Technická 8, 616 00 Brno, Czech Republic
[5] CSIRO Materials Science and Engineering, P.O. Box 218, Lindfield, NSW 2070, Australia

Abstract. Numerical simulation of mixing of argon- and water-plasma species in argon-steam arc discharge has been investigated in thermal plasma generator with the combined stabilization of arc by axial gas flow (argon) and water vortex. Mixing process is described by the combined diffusion coefficients method in which the coefficients describe the diffusion of argon "gas", with respect to steam "gas". Calculations for currents 150–600 A with 15–40 standard liters per minute (slm) of argon reveal inhomogeneous mixing of argon and oxygen-hydrogen species with the argon species prevailing near the arc axis. However, calculations for currents higher than 400 A were not straightforward and a phenomenon of premixing of argon and steam species in the upstream discharge region was predicted from modelling to obtain reasonable agreement with experimental data. Premixed argon-steam plasma has a global impact on the plasma jet parameters near the exit nozzle as well as on the overall arc performance. The results of thermo-fluid fields, species mole fractions and radiation losses from the discharge are presented and discussed. Our former calculations based on the homogeneous mixing assumption differ from the present model in temperature, enthalpy, radiation losses, and flow field. Comparison with available experiments exhibits very good qualitative and quantitative agreements for the radial temperature profiles and satisfactory agreement for the velocity profiles 2 mm downstream of the exit nozzle.

1 Introduction

Thermal plasmas have been widely used as the high temperature energy sources in many applications, such as the gas-tungsten arc welding, gas-metal arc welding, plasma spraying, plasma cutting, plasma metallurgy, plasma waste destruction, or gas-blast circuit breakers to interrupt the electrical current [1,2]. The occurrence of dissociation and ionization in thermal plasmas means that a large number of species are generally present in such gas mixtures. Diffusive mixing of two high-temperature gases is also important, such as the electric arc multicomponent thermal plasma or entrainment of a cold gas into a plasma jet. Diffusion of individual plasma species as well as of the gases with respect to each other is a complex physical phenomenon driven by spatiotemporal gradients of plasma temperature, species number density, pressure, and external forces, such as the electric field. Several processes in

plasma can also lead to the phenomenon of demixing [3,4], i.e. the diffusive separation of the different chemical elements in the plasma.

Numerical models of a plasma mixture of different gases have to consider the diffusion of the gases with respect to each other. The most accurate way to model diffusion is to treat each species separately, and to solve a continuity equation for each species. However, in a plasma mixture containing a large number of species, the number of the corresponding continuity equations and diffusion coefficients will be very large. Because of this complexity, several different approximations have been developed [5–9] that treat diffusion in terms of the binary diffusion coefficients. Murphy [10] developed a method of calculating diffusion coefficients between gases that gives results fully consistent with the full multicomponent diffusion coefficient treatment provided that (1) the gases are homonuclear (i.e. that a molecule of the gas contains atoms of only one chemical element), (2) that they do not react with each other, and (3) that local chemical equilibrium can

[a] e-mail: jenista@ipp.cas.cz

be assumed to exist in a gas mixture. Instead of solving conservation equations for the mass of each species, the species are combined into their parent gases (gas A, gas B), so only one conservation equation (e.g. for gas A) has to be solved. The diffusion coefficients in this approach are linear sums of the ordinary diffusion coefficients. They are called "combined diffusion coefficients" and the method introduced by Murphy [10] is called equally.

The combined diffusion coefficients method has been successfully applied to modelling a wide range of phenomena in thermal plasmas, involving the diffusive mixing and demixing of gases and vapours, such as demixing in atmospheric-pressure free-burning arcs [4,11,12], argon-hydrogen wall-stabilized non-transferred arc [13], argon and nitrogen arc plasmas impinging on a metal target inside a plasma reactor [14], hydrogen-argon radio-frequency plasma torch [15], gas–metal arc welding (GMAW) [16], mixing of air into plasmas [17,18], mixing of ablated material (copper, iron, PTFE) into the arc in circuit breakers [19].

Mixing of argon and steam is being utilized in the so-called hybrid-stabilized electric arc, utilizing a combination of gas and vortex stabilization and developed more than a decade ago at the Institute of Plasma Physics, AS CR, v.v.i. (IPP AS CR, v.v.i.). Its principle is shown in Figure 1. In the hybrid argon–water plasma torch, the arc chamber consists of the short cathode part with the arc stabilization by tangential argon flow, and the longer part, stabilized by water vortex. The arc burns between the cathode, made of a small piece of zirconium pressed into a copper rod, and the water-cooled rotating copper disc anode downstream of the torch orifice. Argon, flowing axially into the discharge chamber, and steam, evaporated from water vortex, create argon-steam (i.e., argon-oxygen-hydrogen) arc plasma, flowing from the discharge chamber to the surrounding atmosphere with high outlet plasma velocities, temperatures ($9000 \, \text{m s}^{-1}$, $26\,000 \, \text{K}$) and plasma enthalpy. The torch exhibits considerably higher input powers and lower mass flow rates ($\sim$200 kW, $0.3 \, \text{g s}^{-1}$) than gas-stabilized arcs (Ar, He; 50 kW, $3 \, \text{g s}^{-1}$). The experiments made on this type of torch [20,21] showed that the plasma mass flow rate, velocity and momentum flux in the jet can be controlled by changing the mass flow rate of argon in the gas-stabilized section, whereas thermal characteristics are determined by the processes in the water-vortex-stabilized section.

According to the author's knowledge there is no other (civil) research group investigating the plasma generated in the same configuration, i.e. in the torch by evaporation of a liquid with a strong tangential velocity component. There are only a few researches using plasma torches with a configuration creating a swirl plasma velocity component, for example [22–24], for the purpose of future industrial application such as thermal plasma chemical vapor deposition or plasma chemistry.

The hybrid-stabilized electric arc has been used at IPP AS CR, v.v.i., in the plasma spraying torch WSP®H (160 kW) for spraying metallic or ceramic powders (TiO_2, Al_2O_3, $ZrSiO_4$, W-based, Ni-based alloys, Al, steel) injected into the plasma jet. Some of the important studies of physical and chemical processes in materials

after their interaction with plasma can be found, e.g., in [25–32]. Another field of utilization of this arc is pyrolysis and gasification of waste streams with the aim to obtain a high content of a combustible mixture of hydrogen and carbon monoxide (the so-called syngas) [33–37] in an experimental plasmachemical reactor PLASGAS. A parametric numerical study of biomass gasification processes in PLASGAS has been also carried out [38], based on various diameters of wooden particles.

Some of our previous numerical simulations analyzed flow regimes, thermal and electrical characteristics and power losses in the argon-steam hybrid-stabilized arc [39]. Calculations have been carried out for the interval of currents 300–600 A and for argon mass flow rates between 22 and 40 slm. Two radiation models have been employed in our former calculations, the net emission coefficient and partial characteristics methods [40–43], as well as the Large-Eddy-Simulation (LES) turbulent model [44–46] to check possible deviations from the laminar flow assumption. The results of simulations confirmed, apart from the other results, a negligible effect of the tangential motion of plasma on the overall arc performance [47,48], existence of transition to supersonic flow regime at the plasma jet near the outlet nozzle orifice for currents higher than 400 A [49–51], and quasi-laminar plasma flow structure near the exit nozzle [45,46,52]. Comparison with available experimental data showed very good agreement for the radial temperature profiles and satisfactory agreement for the radial velocity profiles [50,51]. Evaluation of the Mach number from the experimental data for 500 and 600 A confirmed the existence of the supersonic flow regime [50,51] predicted in simulation.

It has already been confirmed from spectroscopic experiments made by Hrabovský et al. [20], that argon and water plasma species are mixed only partially in the plasma jet flowing from the discharge chamber, and, in addition, that mixing of individual components depends also on arc current. Since we cannot observe directly the arc discharge in the chamber, modelling is the only way to confirm if argon and steam plasma species are mixed fully, partially, or if they are even demixed. The quasi-laminar plasma flow [45,46,52] with steep radial gradients of temperature, particle number density and velocity can induce significant diffusion of species. Our latest simulation [53], especially focused on the effect of mixing of argon and steam plasma species for 150–400 A and for argon mass flow rates between 15 and 22.5 slm, showed inhomogeneous mixing with argon species dominant in the central regions of the arc and water ones in the arc fringes. Distribution of species in the plasma jet substantially influences the flow and the thermal transport in plasma, so that one can expect an impact on heat transport to the anode surface and on the physics of anode processes, such as the restrike mode of the anode attachment and arc shunting, studied in [54].

The present study is an extension of our previous simulation [53] for the range of currents from 400 to 600 A and argon mass flow rates from 22.5 to 40 slm. It has to be pointed out that the calculation was not trivial and straightforward as one boundary condition had to be modified in order to achieve physically reasonable results
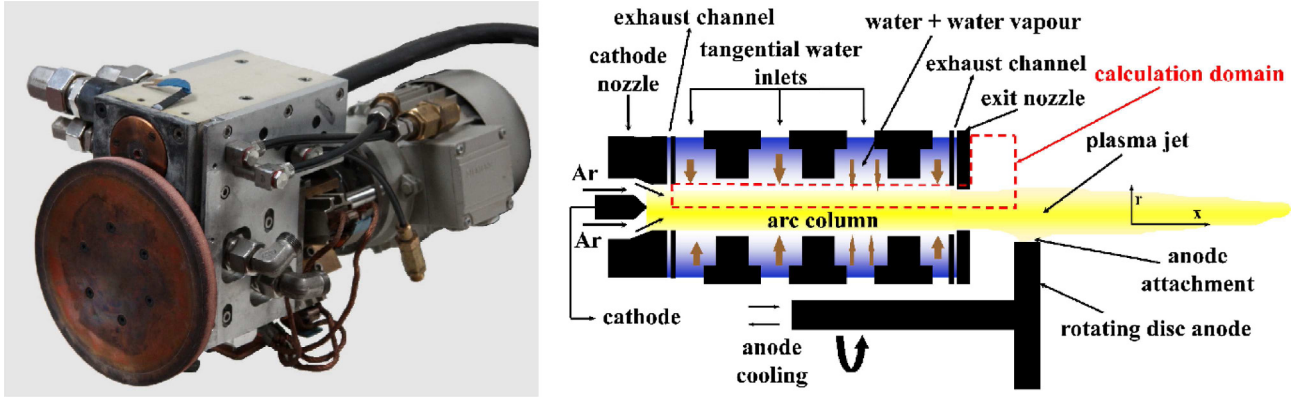
Fig. 1. The plasma spraying torch WSP®H with hybrid stabilization (left), i.e. the combined stabilization of arc by axial gas flow (Ar or N₂) and water vortex. Principle of hybrid plasma torch WSP®H with combined gas (Ar) and vortex (water) stabilizations (right). The calculation domain is shown by a dashed line.

comparable with experiments. It is shown that the way of mixing of argon and steam plasma species in the upstream region strongly influences properties of the plasma jet flowing from the chamber as well as the overall arc performance (energy balance). The combined diffusion coefficients method [10,55] is applied here again as a species mixing model with diffusion processes due to generally all possible physical mechanisms, i.e. due to gradients of mass density, temperature, pressure, and an electric potential. The results are compared with our former model neglecting species mixing [50,51] and with available experiments.

We begin the paper with the description of the physical model in Section 2, boundary conditions in Section 3, and the most important findings in Section 4, including the comparison with our former results [50,51] and available experiments. Our conclusions are given in Section 5.

2 Physical model

2.1 Description of the model

The following assumptions for the model are adopted:

(1) the numerical model is two-dimensional (2-D) with the discharge axis being the axis of symmetry;
(2) plasma flow is considered to be generally turbulent and compressible in the state of local thermodynamic equilibrium (LTE);
(3) only a self-generated magnetic field by the arc itself is considered;
(4) the partial characteristics method for radiation losses from the arc is employed;
(5) gravity effects are negligible;
(6) processes in the cathode potential fall were omitted.

As was mentioned earlier [53], the two-dimensional assumption is guaranteed in major part of the calculation domain due to (a) cylindrical symmetry of the discharge chamber setup, (b) tangential injection of water through the holes along the circumference of the cylindrical discharge chamber and (c) the flexible distance between the nozzle exit and the anode. The tangential velocity component has a negligible effect on the overall arc performance [47,48] and its impact on a plasma flow is through the centrifugal force in the radial velocity equation, and through a contribution to the viscous dissipation in the energy equation. For the reason of generality, distribution of the tangential velocity component in the discharge is interpolated from our different model [47,48] and implemented as a source term in the momentum equation.

It was found [52] that the plasma flow can be considered as quasi-laminar for the operating conditions and simplified discharge geometry in the present study. This fact ensures that turbulence does not overwhelm or smear diffusion processes which is the subject of this study. Nevertheless, turbulence is applied here for the purpose of generality in the numerical model. The evidence of a quasi-laminar plasma jet flowing from the discharge chamber was also confirmed by our experiments for currents up to 600 A. The plasma flow is generally compressible with the Mach number up to 1.4 and solved by appropriate compressible flow solver.

The electric potential drop between the cathode and the outlet nozzle reaches up to ∼200 V so that the cathode fall with the drops of several volts cannot influence substantially the overall results.

The complete set of conservation equations representing the continuity equations for density and species, and the transport of the electric charge, momentum and energy of such plasma can be written in the vector notation as follows:

continuity equation:

$$\frac{\partial}{\partial t}\rho + \nabla \cdot (\rho \vec{u}) = 0. \tag{1}$$

Momentum equations:

$$\frac{\partial}{\partial t}(\rho \vec{u}) + \nabla \cdot (\rho \vec{u} \vec{u}) = -\nabla p + \nabla \cdot \vec{\vec{\tau}} + \vec{j} \times \vec{B},$$

$$\tau_{ij} = \eta \left(\frac{\partial u_i}{\partial x_j} + \frac{\partial u_j}{\partial x_i} - \frac{2}{3}\delta_{ij}\frac{\partial u_l}{\partial x_l} \right). \tag{2}$$

Energy equation:

$$\frac{\partial e}{\partial t} + \nabla \cdot [(e+p)\,\vec{u} - \lambda \nabla T] = \vec{j} \cdot \vec{E} + \Phi_{diss} - \dot{R}. \quad (3)$$

Charge continuity equation:

$$\nabla \cdot (\sigma \nabla \Phi) = 0. \quad (4)$$

Species continuity equation (species conservation equation):

$$\frac{\partial}{\partial t}\left(\rho\overline{f_A}\right) + \nabla \cdot \left(\rho\vec{u}\overline{f_A}\right) = -\nabla \cdot \overline{\vec{J_A}}. \quad (5)$$

Equation of state:

$$p = \rho R_g T. \quad (6)$$

In equations (1)–(6), ρ is the mass density, $\vec{u}$ the velocity vector containing the axial (u) and radial (v) velocity components, p the pressure, $\vec{\vec{\tau}}$ the stress tensor, $\vec{j}$ the current density, $\vec{B}$ the magnetic field, e the density of internal and kinetic energy produced or dissipated in the unit volume, T the temperature, $\vec{E}$ the electric field strength, Φ_{diss} the viscous dissipation term, $\dot{R}$ the divergence of radiation flux (radiation losses), Φ the electric potential, λ and σ are the thermal and electrical conductivities, respectively, and R_g is the specific gas constant. In the species continuity equation (5), $\overline{f_A}$ means the mass fraction of species A (gas A), defined as the sum of the mass fractions of its constituent species and $\overline{\vec{J_A}}$ is the diffusion mass flux of gas A. Details of the species transport will be discussed in next Section 2.2.

Turbulence was modeled by Large-Eddy Simulation using the Smagorinsky sub-grid scale model [44] with the constant values of the Smagorinsky coefficient ($C_S = 0.1$) and the turbulent Prandtl number ($\text{Pr}_t = 0.9$). To suppress turbulence near the walls, a Van Driest damping function $D(y^+, A^+)$ is applied near the walls [44] in the form

$$l_S = C_S \Delta \cdot D(y^+, A^+) = C_S \Delta \left[1 - \exp\left(-y^+/A^+\right)\right], \quad (7)$$

where l_S is the Smagorinsky lengthscale, C_S is the Smagorinsky coefficient, Δ is the filter width, y^+ is the distance from the wall normalized by the viscous lengthscale, and $A^+ = 25$. The eddy viscosity μ_t and the turbulent thermal conductivity λ_t are modeled as [44]

$$\mu_t = l_S^2 \bar{S} = \left(C_S \Delta \cdot D(y^+, A^+)\right)^2 \bar{S}, \quad \lambda_t = c_p \mu_t / \text{Pr}_t. \quad (8)$$

$\bar{S}$ is the characteristic filtered rate of strain and c_p is the specific heat at constant pressure. The filter width Δ is proportional to the grid size with generally nonequidistant spacing Δx_i and Δy_j, defined here as $\Delta = \sqrt{\Delta x_i \Delta y_j}$.

Radiation losses from the argon-steam arc were calculated by the partial characteristics method [41,56] for different mole fractions of argon and water plasma species as a function of temperature and pressure. The advantage of this method is that it directly calculates the reabsorption of radiation in the low-temperature regions of the arc, depending on the distribution of temperature in the discharge.

Continuous radiation due to photo-recombination and *"bremsstrahlung"* processes was included in the calculation as well as discrete radiation consisting of thousands of spectral lines. The shapes of atomic and ionic spectral lines due to natural, temperature (Doppler) and pressure (linear and quadratic Stark, resonance and Van der Waals) broadenings have been considered. A large number of oxygen and argon lines is included in the calculation (the number lines is shown in parenthesis): O (93), O^+ (296), O^{2+} (190), Ar (739), Ar^+ (2781), Ar^{2+} (403), Ar^{3+} (73). In addition, molecular bands of O_2 (Schuman-Runge system), H_2 (Lyman and Verner systems), OH (transition $A^2\Sigma^+ \rightarrow X^2\Pi_i$) and H_2O (several transitions) are also implemented [57]. Hydrogen lines are unfortunately excluded from the radiation model because of numerical problems during the preparation of spectra and the corresponding partial characteristics for this plasma mixture. Absorption coefficient as a function of wavelength was calculated from infrared to far ultraviolet regions. The tables of partial characteristics, used in the code, were generated for 1000–35 000 K and they depend on plasma temperature, pressure (1–3 atm.) and argon mass fraction (0–100).

2.2 Details of the species mixing model

The effect of mixing of plasma species (hydrogen, argon, oxygen) within the hybrid arc discharge is calculated by the combined diffusion coefficients method by A. B. Murphy [10,55]. In this approach, all the plasma species originating from gas 1, i.e., atoms, ions and electrons, form gas A, while all the species created from gas 2 form gas B. Let gas A means argon, and gas B water plasma species. The species continuity equation (5) describes the diffusion of argon species with the divergence of diffusion mass flux of species A ($\overline{\vec{J_A}}$) as a driving "force" for the diffusion. The equation for argon species flux $\overline{\vec{J_A}}$ can be expressed as [58]

$$\begin{aligned}
\overline{\vec{J_A}} = & -\rho\overline{D_{AB}^x}\frac{\overline{m_A m_B}}{\overline{M_A M}}\nabla\overline{f_A} + \rho\overline{D_{AB}^x}\frac{\overline{m_A m_B}}{\overline{M_A M}}\frac{\overline{f_A}}{\overline{M_A}}\nabla\overline{M_A} \\
& -\overline{D_{AB}^x}\frac{\overline{m_A m_B}}{\overline{M_A M}}\frac{\overline{f_A}}{\overline{M}}\nabla\overline{M} + \rho\frac{\overline{m_A m_B}}{\overline{M}^2}\overline{D_{AB}^P}\nabla\left(\ln P\right) \\
& -\rho\frac{\overline{m_A m_B}}{\overline{M}^2}\overline{D_{AB}^E}\nabla\Phi - \overline{D_{AB}^T}\nabla\left(\ln T\right) - \frac{\mu_t}{Sc_t}\nabla\overline{f_A},
\end{aligned} \quad (9)$$

or,

$$\begin{aligned}
\overline{\vec{J_A}} = & -\Gamma_f\nabla\overline{f_A} + \Gamma_f\frac{\overline{f_A}}{\overline{M_A}}\nabla\overline{M_A} - \Gamma_f\frac{\overline{f_A}}{\overline{M}}\nabla\overline{M} + \Gamma_P\nabla\left(\ln P\right) \\
& -\overline{D_{AB}^T}\nabla\left(\ln T\right) - \Gamma_E\nabla\Phi - \frac{\mu_t}{Sc_t}\nabla\overline{f_A},
\end{aligned} \quad (10)$$

when defining the following transport coefficients:

$$\begin{aligned}
\Gamma_f &= \rho\overline{D_{AB}^x}\left[\overline{m_A m_B}/\left(\overline{M_A M}\right)\right], \\
\Gamma_P &= \rho\overline{D_{AB}^P}\left[\overline{m_A m_B}/\left(\overline{M}^2\right)\right], \\
\Gamma_E &= \rho\overline{D_{AB}^E}\left[\overline{m_A m_B}/\left(\overline{M}^2\right)\right].
\end{aligned} \quad (11)$$

In (9)–(11), $\overline{J_A}$ is the argon diffusion mass flux, $\overline{f_A}$ is the mass fraction of gas A (argon), defined as the sum of the mass fractions of its constituent species, ρ is the mass density, $\overline{D_{AB}^X}$, $\overline{D_{AB}^T}$, $\overline{D_{AB}^P}$ and $\overline{D_{AB}^E}$ are the ordinary, temperature, pressure and the electric field strength combined diffusion coefficients respectively, $\overline{m_A}$ is the average molecular weight of heavy particles of gas A (argon), $\overline{m_B}$ is the average molecular weight of heavy particles of gas B (water), $\overline{M_A}$ is the average molecular weight of gas A, including electrons, $\overline{M}$ is the average molecular weight of all particles of gas mixture, Γ_f, Γ_P, Γ_E are the transport coefficients for the ordinary, pressure and electric field diffusions respectively, μ_t is the eddy viscosity, Sc_t is the turbulent Schmidt number. The last term accounts for the diffusion of the argon species due to turbulence. Since our studied arc discharge is quasi-laminar [52] with negligible turbulent effects and the value of μ_t, the proper choice of Sc_t is not required and it is put equal to 1, similarly as in [59].

When combining the first and last terms in equation (10) together into one term, we obtain

$$\overline{J_A} = -\Gamma_{fd}\nabla\overline{f_A} + \Gamma_f\frac{\overline{f_A}}{\overline{M_A}}\nabla\overline{M_A} - \Gamma_f\frac{\overline{f_A}}{\overline{M}}\nabla\overline{M} + \Gamma_P\nabla\left(\ln P\right)$$
$$- \overline{D_{AB}^T}\nabla\left(\ln T\right) - \Gamma_E\nabla\Phi\ , \quad (12)$$

with $\Gamma_{fd} = \Gamma_f + \mu_t\cdot Sc_t^{-1}$ as the transport coefficient for the diffusion term, the other terms in (12) represent the source terms. The first three terms in (12) describe the argon mass diffusion flux due to ordinary diffusion, the other terms present the argon mass diffusion flux due to gradients of pressure, temperature and an electric potential respectively.

By substituting (12) to (5), the species continuity equation (5) takes the final form:

$$\frac{\partial}{\partial t}\left(\rho\overline{f_A}\right) + \nabla\cdot\left(\rho\vec{u}\overline{f_A}\right) =$$
$$\nabla\cdot\left(\Gamma_{fd}\nabla\overline{f_A}\right) - \nabla\cdot\left(\Gamma_f\frac{\overline{f_A}}{\overline{M_A}}\nabla\overline{M_A}\right)$$
$$+ \nabla\cdot\left(\Gamma_f\frac{\overline{f_A}}{\overline{M}}\nabla\overline{M}\right) - \nabla\cdot\left(\Gamma_P\nabla\left(\ln P\right)\right)$$
$$+ \nabla\cdot\left(\overline{D_{AB}^T}\nabla\left(\ln T\right)\right) + \nabla\cdot\left(\Gamma_E\nabla\Phi\right). \quad (13)$$

Since both turbulent and molecular diffusion mechanisms are included in (13) in the Γ_{fd} coefficient, this approach to treat the simultaneous turbulent and molecular diffusion can be called the turbulence-enhanced combined diffusion coefficient method.

If needed, the water species mass fraction $\overline{f_B}$ can be easily calculated from the closure condition $\overline{f_A} + \overline{f_B} = 1$.

2.3 Calculation of the properties of argon–water-vapor plasmas

The composition of the plasma at a given temperature and pressure was calculated by minimizing the Gibbs free

Table 1. Method of calculation of collision integrals.

Interaction	Method
H_2–O_2	Lennard–Jones (12,6) potential [65]
H_2–O	Exponential repulsive potential [65]
H_2–OH	Lennard–Jones (12,6) potential [65]
H–O	Exponential repulsive potential [65]
H_2O–H_2O	Stockmayer (12,6,3) potential [66]
H_2O–H	Buckingham exponential-α:6 potential [67]
H_2O–H_2	Lennard–Jones (12,6) potential [65]
H_2O–O_2	Lennard–Jones (12,6) potential [65]
H_2O–OH	Lennard–Jones (12,6) potential [65]
O_2–O	Collision integral tabulation [68]
O_2–H	Collision integral tabulation [68]
O_2–OH	Lennard–Jones (12,6) potential [65]
OH–OH	Lennard–Jones (12,6) potential [65]
H^+–O	Morse potential [69]
O^+–H	Exponential repulsive potential [69]
O^+–H_2	Charge-exchange data [70]
O^-–H	Charge-exchange data [71]
e–H_2O	Momentum-transfer cross section [72]

energy of the gas mixture, under the constraints of chemical element conservation and zero net charge. The composition, together with the thermodynamic properties of the individual species, was then used to calculate the thermodynamic properties of the plasma. The methods used have been given previously [60]. The species considered in the calculation were: Ar, Ar^+, Ar^{2+}, Ar^{3+}, H, H^-, H^+, H_2, H_2^+, H_2O, O, O^-, O^+, O^{2+}, O^{3+}, O_2, O_2^-, O_2^+, O_3, OH, OH^-, OH^+, electron.

Transport properties were calculated using the Chapman–Enskog method [61–63]. The approaches used, and the methods used to calculate most of the collision integrals have been given previously for interactions involving argon and oxygen species [60] and argon and hydrogen species [64]. However, some collision integrals have been revised because of the availability of improved data. Further, additional collisional integrals were required for interactions between oxygen and hydrogen species. Table 1 lists the methods used to calculate the relevant collision integrals and the sources of the data.

Other collision integrals for neutral species were calculated using the Lennard–Jones (12,6) potential following the methods of André et al. [73] and Hirschfelder et al. [61]. Where data were not available, collision integrals for interactions between unlike neutral species (X–Y interactions) were calculated by interpolating between the collision integrals for the X–X and Y–Y interactions using the method of Svehla and McBride [74]. For other ion-neutral interactions, the polarization potential was used. For the e-OH interaction, the relation given by André et al. [73], allowing the momentum-transfer cross-section to be calculated in terms of the dipole moment of the OH molecule and the momentum transfer cross-section for the e-H_2O interaction, was used.

Combined ordinary diffusion coefficients were calculated as described by A. B. Murphy [10,58]. The coefficients describe the diffusion of argon "gas", with respect to water vapor "gas". Each gas may consist of any number

of species; for example, species including H_2O, OH, O, H, O^+, H^+ and electrons will all be present in the water vapor gas.

As mentioned in introduction, the condition that gases are homonuclear must be fulfilled in the combined diffusion coefficient approach [10]. However, water vapor is heteronuclear; this means that, due to the different diffusion velocities of, for example, H and O atoms, stoichiometry of the water vapor (i.e., 2 atoms of H to 1 atom of O) may not be maintained at every location. The combined diffusion coefficients are calculated assuming stoichiometry is maintained everywhere. Some separation between hydrogen and oxygen species is expected because of their different masses, and ideally the three gases (argon, hydrogen and oxygen) would be treated separately using the recent extension of the combined diffusion coefficient method to three-gas mixtures [75]. We expect that the errors introduced due to this assumption will be small, since the convective flow velocities in this problem are much larger than the diffusion velocities, so any separation of hydrogen and oxygen due to different diffusion velocities will be only a small effect.

The tables of plasma properties were generated for purposes of the code implementation and numerical simulation for temperatures between 500 K and 35 000 K, pressures in the range from 1 to 3 atm., and argon mole fraction between 0% and 100% with the step of 10%. All the plasma properties, combined diffusion coefficients and masses depend in the code on temperature, pressure and argon mass fraction. The effect of inhomogeneous mixing on the discharge behavior is reflected in the dependence of the plasma properties on argon mass fraction.

3 Boundary conditions and the numerical method

The calculation region and the corresponding boundary conditions are presented in Figure 2. The dimensions are 3.3 mm for the radius of the discharge region, 20 mm for the radius of the outlet region and 78.32 mm for the total length. These dimensions agree with the hybrid torch experimental setup. The length and thickness of the outlet region is large enough since no plasma is expected to be present in higher radial distances. The length 20 mm corresponds to the maximum distance from the nozzle exit to the edge of the anode, adjustable in experiments, with the minimum assumed impact on the axial symmetry in the model due to anode attachment and its shunting on the anode surface.

The length of the outlet nozzle shown in Figure 2 corresponds to the experiment but compared to our numerical model there are small radii of the edges in order to reduce thermal erosion of the nozzle. The higher is the arc current, the higher is generally the erosion of the nozzle. The best choice for nozzle material is copper due to its high thermal conductivity and ability to transfer high heat fluxes from the plasma discharge. The nozzle also undergoes additional erosion during the arc operation which is also not considered in the model.
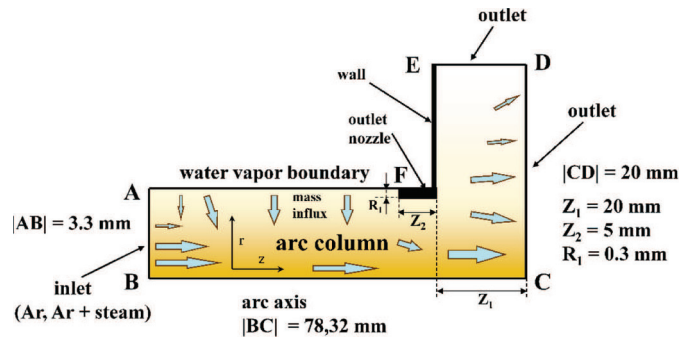

Fig. 2. Discharge area geometry. Inlet boundary (AB) is represented by the nozzle exit for argon or a mixture of argon and steam. The length of the discharge region is 78.32 mm, the length of the outlet Z_1 is 20 mm. Adjacent to the line FE, the outlet nozzle and the wall of the hybrid plasma torch equipment is specified.

It has to be pointed out that the geometry of the chamber presented in Figure 2 is considerably simplified regarding the real geometry. A real technical drawing of the chamber cannot be published. The cylindrical discharge chamber is divided into several sections by the baffles with central holes. Water is injected tangentially into the chamber by three sets of three inlet holes (totally 9 holes) placed equidistantly along the circumference at angles of 120°. The inner diameter of the water vortex is determined by the diameter of the holes in the baffles. Water is usually pumped under pressures of 0.39 MPa (0.6 MPa) with flow rates of 10 L min⁻¹ (16 L min⁻¹). Higher pressures ensure better hydrodynamic stability of the arc. Water/steam circulating in the discharge chamber is being continuously removed by two exhausts (see Fig. 1, exhaust channel).

Description of boundary conditions:

(a) inlet boundary (AB). The nozzle exit for argon or argon-steam plasma. Along this boundary we assume the zero radial velocity component, $v = 0$. Because of the lack of experimental data, the temperature profile $T(r, z = 0)$ and the electric field strength $E_z = -\partial\Phi/\partial z = \text{const.}$ for a given current are calculated at this boundary iteratively from the Elenbaas-Heller equation including the radiation losses from the arc, before the start of the fluid-dynamic calculation itself. The inlet velocity profile $u(r)$ for argon (argon-steam) plasma for the obtained temperature profile $T(r, z = 0)$ is pre-calculated from the axial momentum equation under the assumption of a fully developed flow.

A major difference with regard to our approach in [53] is the choice of a boundary condition for $\overline{f_A}$. Since this boundary is the argon inlet, it is natural to assume that argon mass fraction should be equal to 1 ($\overline{f_A} = 1$) along this boundary. In [53] a modified function in the form

$$\overline{f_A}(z = 0, r) = \left(1 - \frac{r}{|AB|}\right)^{1/100} \qquad (14)$$

was applied in order to avoid a jump discontinuity at the intersection of AB and AF lines ($\overline{f_A} = 0$ at AF line). Here r is the radial coordinate rising from B ($r = 0$) to A ($r = |AB|$). This function provides the values of $\overline{f_A}$ equal

to nearly 1 along the AB line as well as a steep continuous mass fraction gradient near the AB-AF intersection.

Application of this boundary condition was successfully carried out in the calculations for currents 150–400 A with argon mass flow rates 15 and 22.5 slm [53]. Here the calculations for currents below 400 A provide the results that should be expected from the point of view of physics with a very good experimental agreement for 300 A [53], however, it cannot be declared for higher currents. Our results for 400 A and 22.5 slm provided a peak temperature, 2 mm downstream of the nozzle exit, about 2 kK higher compared to the experimental value, and a double-peak velocity profile which nearly fitted the experimental one (see Figs. 18, 19 of [53]). Value of the experimental velocity is obviously underestimated due to the assumption of a constant Mach number across the nozzle radius in the process of experimental evaluation [53], so the numerical velocity for 400 A is expected to be somewhat higher. Further extension of the present model to higher currents (500–600 A) with the boundary condition (14) provided "strange results" far from experiments – relatively high temperatures and low velocities in the outlet region: difference up to 3 kK (500 A, 40 slm) and 4 kK (600 A, 40 slm) for the peak values of temperatures at the discharge axis 2 mm downstream of the nozzle exit, and unrealistic low peak numerical velocities around 4 km s^{-1} for both currents (see Figs. 17 and 18 – calculation old). In addition, velocity practically did not change with current above 400 A and a flow pattern in the nozzle region appeared as clogged. It seems that there is a transition between physically acceptable and non-acceptable solutions around 400 A. After the revision of all boundary conditions and some numerical tests it was finally found that the problem consists in the condition (14), and so there must exist some kind of premixing of argon and steam plasma species along AB in order to obtain numerical results comparable with experiments. It is highly probable that premixing take place in the inlet region close to the AB line as a result of tangential water injection to the discharge chamber at different axial positions and also due to continuous steam and argon removal from the chamber during the arc operation.

At this point some facts have to be explained in more detail. There are two exhausts in the discharge chamber, the first is placed near the outlet nozzle, the second one close to the inlet nozzle for argon, i.e. just close to the AB boundary for argon inlet (see Fig. 1, exhaust channel). This is the principal complication for numerical modelling of processes close to AB. The discharge chamber is a blackbox, we are not able to see inside the chamber and perform any diagnostics. In addition, after the torch operation we can frequently observe some remaining water in the inlet nozzle for argon and in the cathode region, so that water (or steam) is being not only exhausted close to AB but it also penetrates inside the inlet nozzle for argon.

In addition to steam and argon removal from the discharge close to AB there are other problems causing the determination of argon mass fraction profile at AB difficult: (1) part of argon flowing to the discharge is being continuously removed from the discharge by the exhaust pipes together with steam/water. The amount of removed argon is about 50%, but this value is not constant and changes in time (45%–55%), depending on operating conditions and the discharge chamber assembly. (2) There are unpredictable instabilities during the arc operation leading to sudden bursts of water in the exhaust system, observable sometimes near the outlet nozzle. (3) The arc parameters change slightly from experiment to experiment, depending on the specific discharge chamber adjustment (the strength at which the screws are tightened among different parts of the chamber, etc.).

From these considerations it comes out that even if I extend the model with the inlet cathode region (the left side of AB), neglecting the steam penetration into the exhaust and to the cathode region due to its complexity, it will not provide a proper answer for the inlet argon mass fraction profile. To describe all these processes, the model would need to be much more complicated, including the discharge, real geometry of the chamber and also the water-circulating circuit. Evaporation of steam could be directly calculated from radial energy transfer by radiation and conduction, i.e. inclusion of a multiphase model calculating interaction of water molecules with radiation. Such approach is intractable and at this stage the numerical testing of a form of the inlet argon mass fraction profile is a reasonable way to elucidate this problem.

A stronger mixing of steam and argon for higher currents at AB can consist in my opinion in higher overpressure in the chamber and also in a thicker and more hot plasma column, inducing thus stronger interaction with flowing steam/water. Some kind of premixing can be expected also at lower currents than 400 A, nevertheless premixing will be considerably smaller since the boundary condition (14) provides for 300 A the solution with good agreement with our experiments.

During a search for an acceptable inlet argon mass fraction profile I have chosen several kinds of the radial profiles with different amplitudes at the axis (argon mass fractions from 1 to 0.5) and fitted the numerical results obtained with a given $\overline{f_A}$ profile along AB to the corresponding experiments. Comparison was carried out for temperature profiles 2 mm downstream of the nozzle exit and for the electric potential drop inside the chamber from the inlet boundary to the end of the nozzle, with the experimental data published in [20]. Error bars for these quantities are below 15%. Experimental values of velocity were excluded from this analysis due to the simplifying assumption of a constant Mach number across the nozzle radius. Any other physical quantities are not available for comparison because of difficulties linked with fast plasma processes and high-intensity radiation coming out from the discharge. The resulting best-fit $\overline{f_A}$ profile takes the form

$$\overline{f_A}(z=0, r) = 0.8 \cdot \left(1 - \left(\frac{r}{|AB|}\right)^2\right)^{2.5}. \qquad (15)$$

Note that the maximum amplitude is 0.8 so this boundary condition assumes premixing even at the arc axis. Table 2 compares relative difference for the temperature and electric potential for 400–600 A for the best-fit profile (15). The relative difference is defined as

Table 2. Relative differences between calculation and experiment for temperature and electric potential for Profile 1 and 2.

Current & Argon mass flow rate	Temperature rel. diff. [%]		Potential rel. diff. [%]	
	Profile1	Profile2	Profile1	Profile2
400 A, 22.5 slm	5.79	4.44	15.05	12.78
500 A, 22.5 slm	5.14	4.95	11.36	2.71
400 A, 40.0 slm	7.47	3.62	n/a	n/a
600 A, 22.5 slm	8.03	7.06	n/a	n/a
600 A, 40.0 slm	8.99	4.60	n/a	n/a

$$\Delta_\phi\,(\%) = 200 \cdot (\phi_{\mathrm{NUM}} - \phi_{\mathrm{EXP}})\,/\,(\phi_{\mathrm{NUM}} + \phi_{\mathrm{EXP}}) \quad (16)$$

where ϕ_{NUM} is the numerical value of ϕ and ϕ_{EXP} is the corresponding experimental value. For the electric potential, only two single values were compared. In the case of temperature, a set of numerical values along the temperature profile was compared with the corresponding experimental values. The average difference for temperature shown in Table 2 was then obtained as the arithmetic mean of single differences at given radial positions. In Table 2 "Profile 1" means the difference for calculations employing (14), "Profile 2" the difference for (15). One can see the lower relative difference for (15) in all the cases.

In the present calculation, the boundary condition (14) was adopted for currents 150–300 A, the condition (15) otherwise, i.e. for 400–600 A.

(b) Axis of symmetry (BC). The zero radial velocity and symmetry conditions are specified here, i.e. $\partial T/\partial r = \partial u/\partial r = \partial \Phi/\partial r = \partial \overline{f_A}/\partial r = 0$, $v = 0$.

(c) Arc gas outlet plane (CD). The zero electric potential $\Phi = 0$ (the reference value) and zero axial derivatives are defined at CD, i.e., $\partial T/\partial z = \partial u/\partial z = \partial v/\partial z = \partial \overline{f_A}/\partial z = 0$.

(d) Arc gas outlet plane (DE). The zero radial derivatives are defined here: $\partial T/\partial r = \partial u/\partial r = \partial v/\partial r = \partial \Phi/\partial r = \partial \overline{f_A}/\partial r = 0$. Pressure is atmospheric, $p = 1$ atm.

(e) Outlet wall and the nozzle (EF). Specification of no slip conditions for velocities, $u = v = 0$, constant values of E_r, E_z and $\overline{f_A}$ ($\partial \Phi/\partial z = \partial \Phi/\partial r = \partial \overline{f_A}/\partial r = \partial f_A/\partial z = 0$), and $T(r,z) = 773$ K (500° C) for the temperature of the nozzle.

(f) Water vapor boundary (FA). Along this line we specify the so-called "effective water vapor boundary", named in Figure 2 as the "water vapor boundary" with a prescribed temperature of water vapor $T(R = 3.3\,\mathrm{mm}, z) = 773$ K. The details of this assumption and determination of evaporation mass flow rates of water are explained in [50]. The resulting values of mass flow rates based on comparison between simulation and experiment are: $0.228\,\mathrm{g\,s^{-1}}$ (300 A), $0.286\,\mathrm{g\,s^{-1}}$ (350 A), $0.315\,\mathrm{g\,s^{-1}}$ (400 A), $0.329\,\mathrm{g\,s^{-1}}$ (500 A), $0.363\,\mathrm{g\,s^{-1}}$ (600 A) [76]. The magnitude of the radial inflow velocity is calculated from the definition of mass flow rate

$$v(R) = \frac{\dot{m}}{2\pi R \sum_{\Delta z} \rho(R,z)\,\Delta z}, \quad (17)$$

where, $\rho(R,z)$ is a function of pressure and thus dependent on the axial position z, Δz is the distance between the neighboring grid points.

Because no current goes outside of the lateral domain edges, the radial component of the electric field strength is zero, $E_r = -\partial \Phi/\partial r = 0$, as well as the axial velocity component ($u = 0$) and argon mass fraction ($\overline{f_A} = 0$, steam evaporation boundary).

Since the axial component of the current density j_z in the discharge is much higher than the radial one j_r we assume only the tangential component of the self-generated magnetic field by the arc itself

$$B_\vartheta(r,z) = \frac{\mu_0}{r} \int_0^r j_z(r,z)\,r\mathrm{d}r, \quad (18)$$

where μ_0 is the vacuum permeability and $j_z(r,z) = -\sigma(r,z)\partial \Phi/\partial z$.

Spatiotemporal integration of discretized equations (1)–(5) is done by LU-SGS (Lower–Upper Symmetric Gauss-Seidel) algorithm [77], belonging to the group of the density-based methods [78], coupled with the Newtonian iteration method. The compressible phenomena are resolved accurately by the Roe flux differential method [79] coupled with the third-order MUSCL-type (Monotone Upstream-centred Schemes for Conservation Laws) TVD (Total Variation Diminishing) scheme [80,81] for the convective term. The electric potential from (4) is solved by the TDMA (Tri-Diagonal Matrix Algorithm) line-by-line method, including the block correction technique for speeding up the convergence. Under-relaxation is employed to avoid a numerical divergence.

From (1)–(5) we obtain ρ, $\rho\vec{u}$, e, Φ and $\overline{f_A}$. Pressure is determined from the internal energy $U(p, T, \overline{f_A}) = e(p, T, \overline{f_A}) - 0.5\rho\,|\vec{u}|^2$ and temperature is calculated from the equation of state (6) $p/\rho = R_g(p, T, \overline{f_A}) \cdot T$, using the pre-calculated values of the product $R_g(p, T, \overline{f_A}) \cdot T$ as a function of temperature, pressure and argon mass fraction in the mixture. Tables of plasma properties, calculated by A. B. Murphy as described in Section 2.3, have been used in the code and called in an iterative procedure to generate a final steady state solution.

The computer in-house program is written in the FORTRAN language. The task has been solved on an oblique structured grid with nonequidistant spacing. The total number of grid points equals 103 713, with 543 and 191 points in the axial and radial directions, respectively. Compared to [53] the number of points in the radial direction is higher, in the axial direction smaller. Since the highest temperature and concentration gradients occur in the radial direction, a rarefied grid in the axial direction will not influence much the solution. These

grid adjustments have been done for the sake of saving a computer time in many runs. Our numerical tests confirmed that the solutions for 150–300 A with 15–22.5 argon slm differ negligibly from those in [53].

4 Results and discussion

4.1 Basic results

Calculations have been carried out for currents 150, 250, 300, 400, 500 and 600 A. Mass flow rate for water-stabilized section of the discharge (i.e. evaporation of steam) was taken for 300–600 A from our previously published work [76,82], in order to make a consistent comparison of the results with our former calculations for both the inhomogeneous and homogeneous mixing models. Evaporation was determined there iteratively as a minimum difference between the numerical and experimental outlet quantities. It is questionable if evaporation rate of steam will be the same also for this improved numerical model with inhomogeneous argon species mixing. The presence of argon in the central arc region, due to its different radiative properties as well as enthalpy with respect to oxygen and hydrogen plasma, slightly decreases plasma temperature and decreases radiative flux in central parts of the discharge with prevailing argon species. There is not so large difference in reabsorption of radiation in colder arc fringes between inhomogeneous and homogeneous models [53], Figure 11, and about 15% difference with pure water arc discharge. The thickness of water-vapor region (which is only partially included in the model) is influenced by the presence of argon but the mechanism of transferring energy by radiation and conduction for evaporation is unknown to us and it is unclear if these phenomena influence the rate of steam evaporation to large extent. The effect is probably not so large, otherwise it would be indicated by measurements as considerably higher/lower values of temperature and velocity of the plasma jet. Small changes in evaporation rate will influence rather plasma velocity than temperature and electrical potential which have been taken for comparison in this study.

Evaporation of steam for 150–250 A was determined as a logarithmic extrapolation from the values for currents 300–600 A. The resulting values of steam mass flow rates are 0.111 g s^{-1} (150 A), 0.206 g s^{-1} (250 A), 0.228 g s^{-1} (300 A) and 0.315 g s^{-1} (400 A), 0.329 g s^{-1} (500 A) and 0.363 g s^{-1} (600 A).

Argon mass flow rates taken into consideration here and corresponding to experiments are 15, 22.5, 27.5, 32.5 and 40 slm. As in [53] we assume in this calculation that argon mass flow rate present in the discharge equals one-half of argon mass flow rate at the torch inlet (i.e. for 40 slm we take 50% of this amount, etc.) because part of argon is being removed from the discharge chamber, as confirmed in experiments. The amount of removed argon fluctuates in time (∼45–55%) and we take some average value.

The basic results are presented in Figures 3–18. The orientation and geometry of the calculation domain in Figures 3–10, 14 correspond to those in Figures 1 and 2.

Since the ratio of the axial to radial dimensions of the calculation domain is ∼24 (aspect ratio) the scaling of the radial and axial coordinates is not proportional in order to clearly display the contours inside the discharge region. Argon (or argon-steam mixture) flows axially into the domain, whereas steam flows in the radial direction from the "water vapor boundary" in accordance with Figure 2. Since the steady states obtained for all the operating conditions exhibit time and space fluctuations of all the physical parameters (temperature, velocity, Mach number, pressure, etc.) in a plasma plume at the outlet region, all the plots shown here are the time-averaged plots over one fluctuating quasi-period [53].

Isopleths of argon mole fractions for 150, 300, 400 and 600 A in Figure 3 clearly display inhomogeneous mixing of plasma species in the discharge. It can be said that for all currents argon species are dominant in the central regions of the arc, water ones in the arc fringes. The principal difference in the shape of the contours for lower currents, up to 300 A, and for higher currents, is caused by application of different boundary conditions for argon mass fraction at the argon inlet boundary: (14) below 300 A, and (15) otherwise. For currents higher than 400 A, contours of argon mole fraction are nearly parallel in the axial direction, and the mole fraction of argon in the arc fringes is lower than for currents below 300 A. The shape of the contours is obviously also influenced by the increasing evaporation rate of steam along the water vapor boundary with the current, i.e., 0.111 g s^{-1} (150 A), 0.228 g s^{-1} (300 A), 0.315 g s^{-1} (400 A), 0.363 g s^{-1} (600 A), leading to a more squeezed argon-prevailing species region.

Despite relatively low argon mole fraction values in the outlet nozzle region, the corresponding argon mass fractions, plotted in Figure 4 for 150 and 600 A, show relatively high values within the discharge (150 A) and in the axial arc region (600 A). The maximum values close to the discharge axis at the axial position around 58 mm, corresponding to the end of the outlet nozzle, are 0.65 (150 A) and 0.75 (600 A). Argon mass fraction contours can be converted from the mole fractions by a simple formula

$$\overline{f_A} = \overline{X_A} \frac{\overline{M_A}\left(p, T, \overline{X_A}\right)}{\overline{M}\left(p, T, \overline{X_A}\right)}, \tag{19}$$

where $\overline{f_A}$ is the mass fraction, $\overline{X_A}$ is the mole fraction, $\overline{M_A}$ is the average molecular weight of argon, including electrons and $\overline{M}$ is the average molecular weight of all particles of gas mixture. Since the masses $\overline{M_A}$ and $\overline{M}$ depend at higher temperatures on pressure, temperature and argon mass fraction, obtaining of $\overline{f_A}$ is not straightforward and interpolation in the tables of properties is needed.

Figures 5 and 6 show temperature, enthalpy, velocity and the Mach number contours for 150 and 600 A with 27.5 slm of argon. Temperature field is nearly fully developed inside the discharge, i.e., depending only on the radial coordinate. Little pronounced temperature maxima are obvious for 150 A at the arc axis close to the position of 1 cm and near the exit nozzle. For 600 A temperature increases gradually along the axis as far as the outlet region behind the nozzle where one can see a quasi-periodic "wavy-structure" indicating the existence
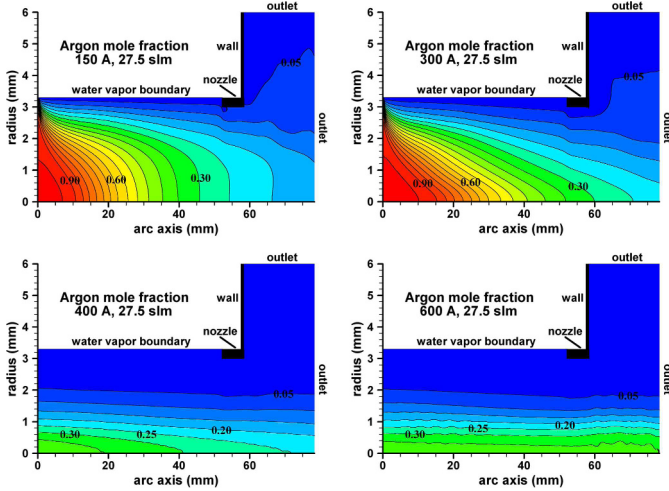
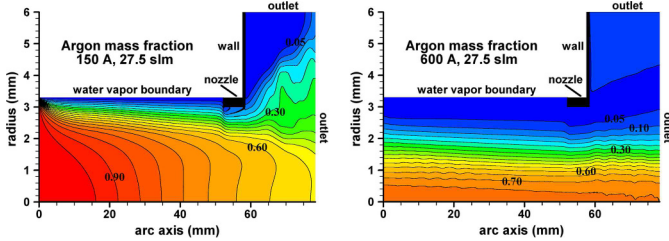**Fig. 3.** Argon mole fraction contours for 150–600 A and 27.5 slm of argon. Contour increment is 0.05.

Fig. 4. Argon mass fraction contours for 150 and 600 A and 27.5 slm of argon. Contour increment is 0.05.

Fig. 5. Temperature and enthalpy contours for 150 and 600 A and 27.5 slm of argon. Steam mass flow rates are $0.111 \, \mathrm{g \, s^{-1}}$ (150 A) and $0.363 \, \mathrm{g \, s^{-1}}$ (600 A). Contour increments are 1000 K for temperature and $1.6 \, 10^7 \, \mathrm{J \, kg^{-1}}$ (150 A) and $2 \, 10^7 \, \mathrm{J \, kg^{-1}}$ (600 A) for enthalpy.

Fig. 6. Velocity and the Mach number contours for 150 and 600 A and 27.5 slm of argon. Steam mass flow rates are $0.111 \, \mathrm{g \, s^{-1}}$ (150 A) and $0.363 \, \mathrm{g \, s^{-1}}$ (600 A). Contour increments are $100 \, \mathrm{m \, s^{-1}}$ (150 A) and $500 \, \mathrm{m \, s^{-1}}$ (600 A) for velocity, and 0.04 (150 A) and 0.10 (600 A) for the Mach number.

of a supersonic plasma flow region. The thickness of the low-temperature region with temperatures below 10 kK decreases with the current. It starts around the radial positions of 1.8 mm for 150 A and 2.6 mm for 600 A.

Distributions of enthalpy within the discharge show fundamentally different pictures for both currents. For 150 A there is a maximum at the axis near the outlet of the order of $10^8 \, \mathrm{J \, kg^{-1}}$. Since the enthalpy increases inside the discharge towards the higher axial positions and the plasma temperature is nearly uniform along the axis, it is obvious that the enthalpy is strongly influenced by argon mole fraction and the highest enthalpy values occur in the regions with lower content of argon plasma species. For 600 A the enthalpy maxima are shifted out of the arc axis to the radial positions between 1.5 and 2 mm where a region with a low argon mole fraction exists. Since the enthalpy of argon plasma is much lower than that of water plasma, the enthalpy decreases towards the arc axis (due to a higher argon mole fraction).

Velocity generally increases towards the outlet and its maximum value reaches around $1300 \, \mathrm{m \, s^{-1}}$ for 150 A. The corresponding Mach number contour exhibits the subsonic plasma flow with the maximum of about 0.4 in the outlet nozzle region. On the contrary, for 600 A we can clearly see a supersonic under-expanded flow structure in the near-outlet region with nicely distinguished shock diamonds with a maximum velocity of about $8000 \, \mathrm{m \, s^{-1}}$ and the Mach number 1.3.
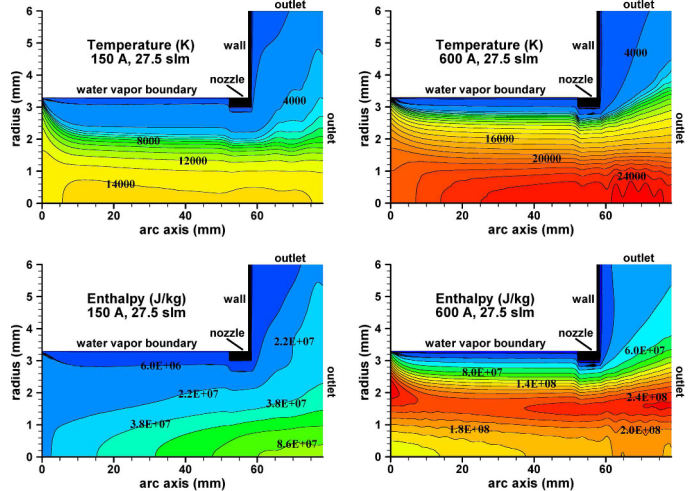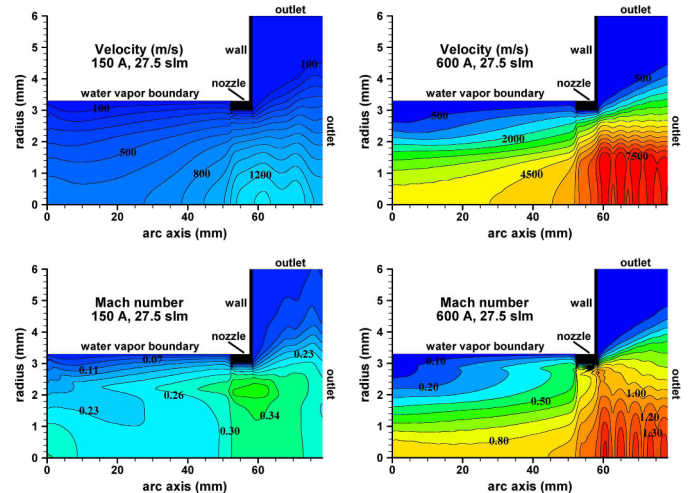
Following Figures 7 and 8 display the combined diffusion coefficients for 150 and 600 A and 27.5 slm of argon. The combined temperature diffusion coefficient $\overline{D_{AB}^T}$ (where $A = Ar$ and $B = H_2O$) shown in Figure 7 depends strongly on both temperature and mole fractions of Ar and H_2O. Similarly to Ar–O_2 and Ar–H_2 mixtures, $\overline{D_{AB}^T}$ is largest at a temperature of 14 000 to 15 000 K and approximately equal mole fractions of Ar and H_2O [60,64]. Comparing the distributions of $\overline{D_{AB}^T}$ and the temperature and argon mole fraction in the plasma torch, it can be seen that for 150 A, $\overline{D_{AB}^T}$ is largest on axis at axial positions between 24 and 44 mm. This corresponds to the maximum
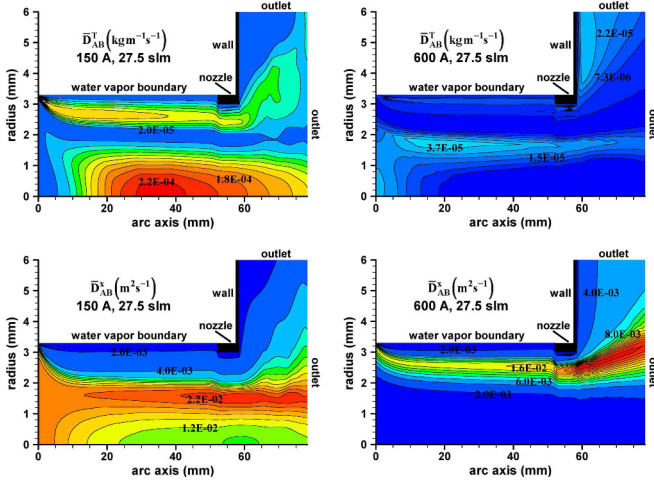
Fig. 7. The combined temperature and ordinary diffusion coefficients $\overline{D_{AB}^T}$ (top) and $\overline{D_{AB}^X}$ (bottom) for 150 and 600 A and 27.5 slm of argon.

Fig. 8. The combined pressure and electric field diffusion coefficients $\overline{D_{AB}^P}$ (top), $\overline{D_{AB}^E}$ (bottom) for 150 and 600 A and 27.5 slm of argon.

temperature (between 14 000 and 15 000 K) and an argon mole fraction between 0.33 and 0.50. For 600 A, $\overline{D_{AB}^T}$ contours are fundamentally different from those for 150 A, due to a changed argon mole fraction distribution, with the values of about one order lower. The local maximum values occur for temperatures between 8–10 kK, argon mole fractions 5–10%, and the radial positions between 1.6 and 1.8 mm.

The combined ordinary diffusion coefficient $\overline{D_{AB}^x}$ (Fig. 7–bottom) depends mainly on temperature, with only a weak dependence on mole fraction. Similarly to Ar–O$_2$ and Ar–H$_2$ mixtures, the maximum occurs around 11 000 to 12 000 K [60,64]. Comparing the distributions of $\overline{D_{AB}^x}$ and temperature in the plasma torch, it can be seen that $\overline{D_{AB}^x}$ is largest at radius 1.6 mm for a current of 150 A, and 2.4–2.6 mm for 600 A, corresponding in all cases to temperatures of around 11 000 to 12 000 K. The maximum values of $\overline{D_{AB}^x}$ are comparable for both currents. Further, it can be seen that $\overline{D_{AB}^x}$ is not strongly dependent on the argon mole fraction (Fig. 3).

The combined pressure diffusion coefficient $\overline{D_{AB}^P}$ (Fig. 8–top) also depends strongly on both temperature and mole fractions of Ar and H$_2$O. For Ar–O$_2$ mixtures, $\overline{D_{AB}^P}$ is largest at a temperature of 12 000 K and about 50 mol% Ar [60], while for Ar–H$_2$ mixtures, $\overline{D_{AB}^P}$ is largest at a temperature about 11 000 K and about 25 mol% Ar [64]. $\overline{D_{AB}^P}$ is much larger for Ar–H$_2$ mixtures than for Ar–O$_2$ mixtures, so $\overline{D_{AB}^P}$ for Ar–H$_2$O mixtures is close to that for Ar–H$_2$ mixtures. Comparing the distributions of $\overline{D_{AB}^P}$ and the temperature and argon mole fraction in the plasma torch, it can be seen that for 150 A, $\overline{D_{AB}^P}$ is largest at a radius of about 1.6 mm at axial positions between 40 and 65 mm. This corresponds a temperature of around 11 000 K and an argon mole fraction between approximately 0.20 and 0.35. For 600 A, $\overline{D_{AB}^P}$ contours are again fundamentally different from those for 150 A with
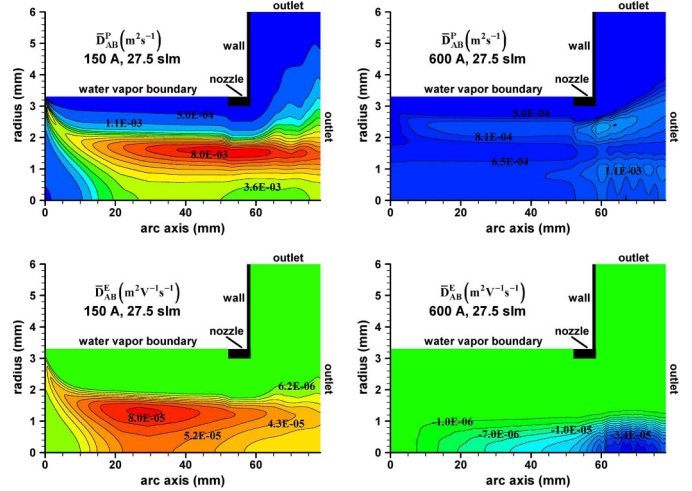
the local maximum values in the arc fringes where the water plasma species prevail.

The combined electric field diffusion coefficient $\overline{D_{AB}^E}$ (Fig. 8–bottom) for Ar–H$_2$ mixtures is largest at a temperature about 12 000 K and approximately equal mole fractions of Ar and H$_2$ [64]. No data has been published for Ar–O$_2$ mixtures. Comparing the distributions of $\overline{D_{AB}^E}$ and the temperature and argon mole fraction in the plasma torch, it can be seen that the maximum values of $\overline{D_{AB}^E}$ correspond to the positions at which the temperature is around 12 000 K and the argon mole fraction is 0.5 for 150 A. $\overline{D_{AB}^E}$ for 600 A exhibits negative values in the arc core (demixing due to the electric field) with the minimum value about -4×10^{-5} m^2 V^{-1} s^{-1} and low positive values in the other parts of the discharge. Since the axial electric field strength is of the order of 1000 V m^{-1} the diffusion of species due to this mechanism can be regarded as negligible in comparison to the other diffusions.

Figure 9 presents the mass fluxes of argon and steam plasma species in the discharge, i.e., the product of density of argon (or water) species and plasma velocity. Mass flux of argon species for lower current is higher in the hot axial region near the argon inlet boundary (Fig. 2, AB line) and in the region parallel with the axis placed radially around 2.2 mm. For 600 A the mass flux is higher and nearly copies the argon mole fraction contours for 600 A. On the contrary, mass flux of steam species is highest at low temperature regions in the arc fringes for both currents. The high values close to the outlet nozzle are the effect of higher plasma velocity and density around the nozzle.

The effect of increased argon mass flow rate on the arc performance is demonstrated in Figure 10 for 250 and 500 A with argon mass flow rates 15 and 40 slm. A higher argon mass flow rate results generally in a higher content of argon species in the discharge, namely in the axial region. For example, the contour line 0.6 of mole fraction for 15 slm (250 A) is positioned at 15 mm at the
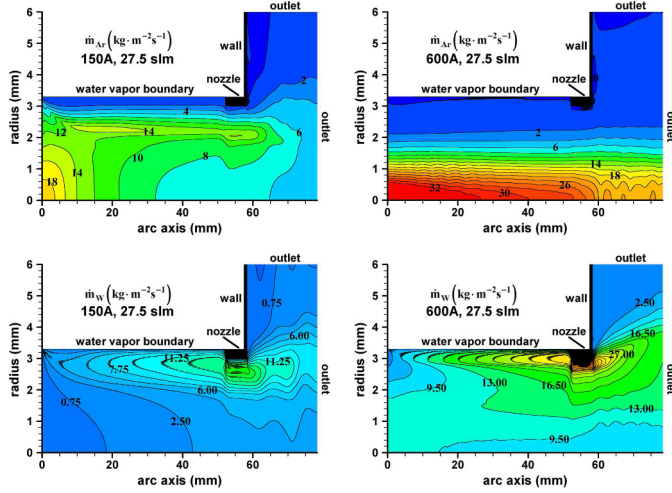
Fig. 9. Mass flux of argon (top) and water (bottom) species for 150 and 600 A and 27.5 slm of argon.
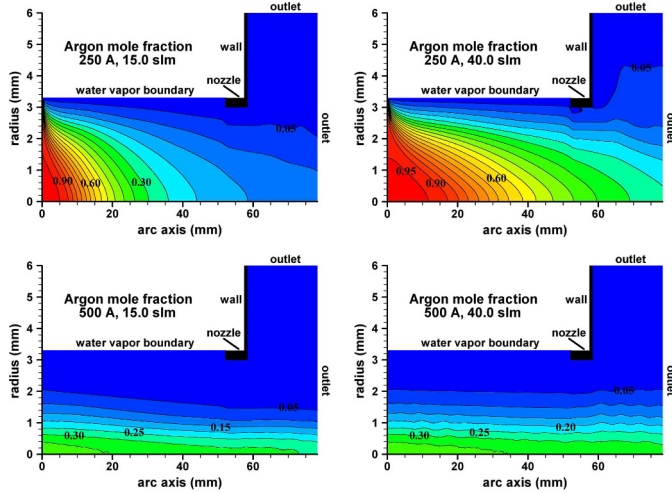

Fig. 10. Argon mole fraction contours for 250 and 500 A, and 15.0 and 40.0 slm of argon. Contour increment is 0.05.

axis, while the same line has an axial position 35 mm for 40 slm. Increase of argon mass flow rate for 500 A results in nearly parallel argon mole fraction contours with the axis and slightly higher values in the radial direction.

Next two Figures 11 and 12 show argon mole fraction, reabsorption of radiation in the discharge, temperature and velocity in the argon mass flow rate vs current plot. Each dot in these plots represents one calculation and the magnitude of a given quantity is demonstrated by a size of the dot. Values of the argon mole fraction, temperature and velocity are taken at the arc axis 2 mm downstream of the nozzle exit. Reabsorption of radiation is a global value calculated here as the ratio of the negative and positive contributions of the divergence of radiation flux, integrated through the discharge volume. The argon mole fraction range is between 0.15 and 0.42 with the maximum values 0.29–0.42 for 40 slm of argon. For currents 150–400 A the argon mole fractions are monotonously increasing with increasing

argon mass flow rate, for the higher currents this tendency is not observed. Reabsorption of radiation ranges between 41 and 60%, for currents 150-400 A it decreases for about 6% with increasing argon mass flow rate, but it slightly increases for 500–600 A. The dots contained in a rectangle show values already presented in [53]. The calculated ranges of temperatures and velocities are 14.3–26.5 kK and 1.0–8.7 km s^{-1}, temperature at the nozzle exit generally increases with current and with decreasing argon mass flow rate, velocity increases with the increase of both variables. The direction of increase is indicated by the arrows in both plots.

Figure 13 illustrates the radial profiles of mole fractions of dominant species at the nozzle exit for 150 and 500 A and for 32.5 slm of argon; Ar$^+$, H$^+$, O$^+$, e$^-$, Ar, H, O, OH. These profiles were obtained by interpolating in the set of LTE tables for the plasma composition by A. B. Murphy based on the calculated radial profiles of temperature, argon mass fraction and pressure for each current at the nozzle exit. At a lower current, ions as well as Ar, H and O atoms are present in the arc core region. The peaks of H and O atoms are located around 2 mm from the arc axis. At a higher current, ions dominate in the arc core and all the atoms are shifted to the arc fringes with lower temperatures. The peaks of H and O atoms now occur around 2.6 mm.

4.2 Comparison with our former calculations

In this subsection we compare the results of the present model with our previous one [51] which neglects the mixing process and assumes that argon mass fraction is constant within the whole calculation domain and determined easily from the ratio of argon to steam mass flow rates. Comparison of temperature and velocity profiles outside of the discharge chamber with available experiments is presented in the last two plots. Similarly as in [53], results obtained by the present inhomogeneous mixing model will be denoted as IM (inhomogeneous model), results obtained by our former model as HM (homogeneous model). In order to be consistent with the present IM model and for the purpose of comparison, the former HM model [51] was recalculated with the same plasma properties by Murphy used here.

Plots of temperature, enthalpy, velocity and the Mach number within the discharge for HM for 600 A and 27.5 slm of argon are illustrated in Figure 14. For comparison see the same physical quantities for IM shown in Figures 5 and 6. The major differences in temperature field for HM with respect to IM are somewhat higher temperatures at the arc axis as well as a thinner arc fringe (a low-temperature region). Enthalpy contours follow approximately the temperature ones with their maximum values at the axis. There is no shift of the enthalpy peak values for HM out of the arc axis as in the case of IM, as a result of a high argon mole fraction in the axial region. The peak velocities at the outlet region are ∼8.5 km s^{-1} for HM, while 7.5 km s^{-1} for IM, nevertheless the Mach number is higher for IM (∼1.3) and so the supersonic Mach disks are more pronounced.
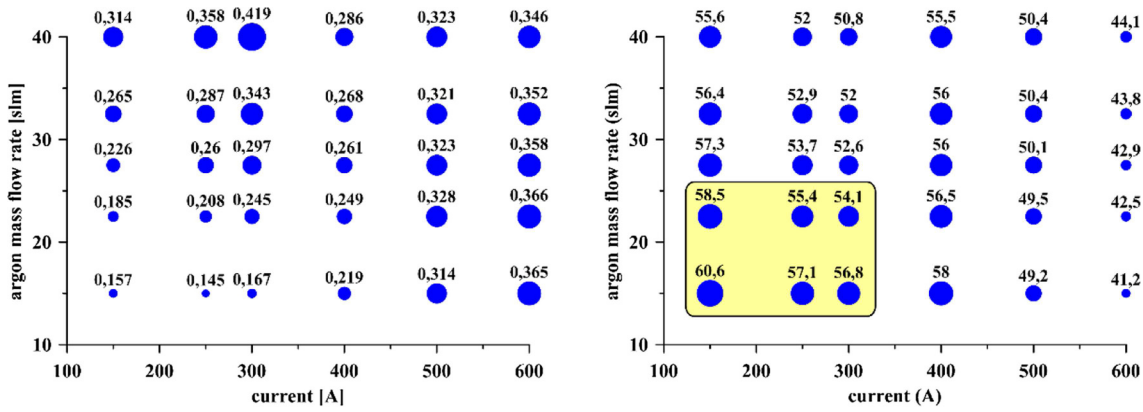
Fig. 11. Left-argon mole fraction 2 mm downstream of the nozzle exit, right-reabsorption of radiation within the discharge in %, both in dependence on argon mass flow rate and current.
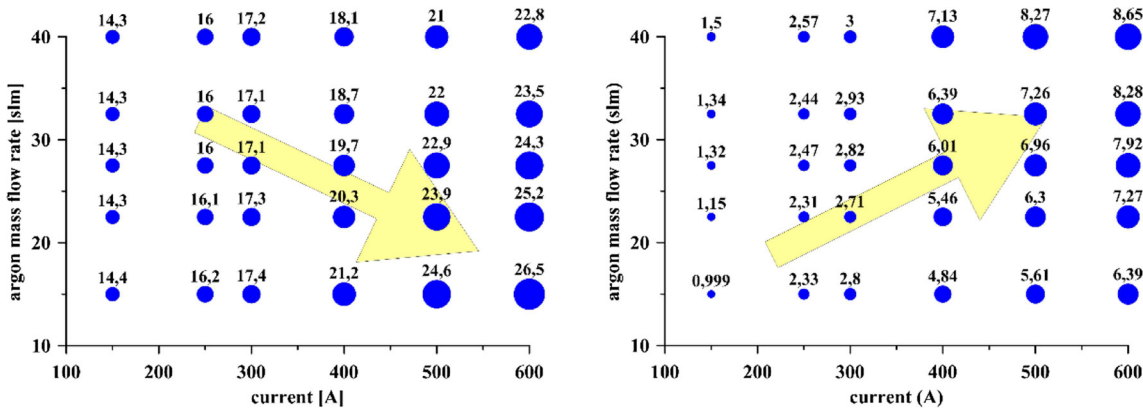

Fig. 12. Left-temperature [kK], right-velocity [km s^{-1}], 2 mm downstream of the nozzle exit in dependence on argon mass flow rate and current. The arrows show the direction of increase.
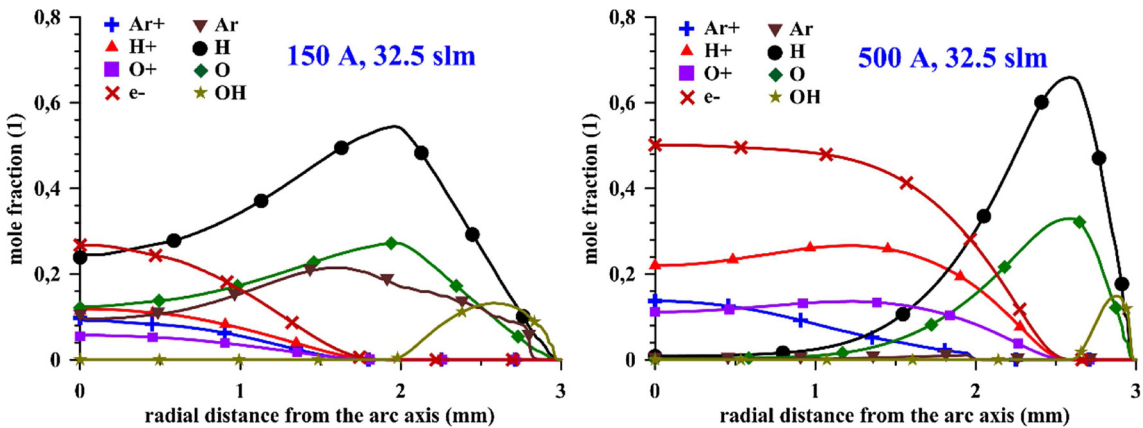

Fig. 13. Radial profiles of dominant plasma species for 150 and 500 A and 32.5 slm of argon at the nozzle exit.

The effect of inhomogeneous mixing model on the arc temperature, reabsorption of radiation within the discharge, velocity and the Mach number is displayed in Figures 15 and 16. Here the values of temperature, velocity and the Mach number are taken again at the axial position 2 mm downstream of the nozzle exit, reabsorption comes out from the overall calculation. The contour plots show a relative difference Δ_ϕ of a given quantity ϕ defined as

$$\Delta_\phi\,(\%) = 200 \cdot (\phi_{IM} - \phi_{HM})\,/\,(\phi_{IM} + \phi_{HM}),\qquad(20)$$

where ϕ_{IM} is the value for the IM model, ϕ_{HM} is the corresponding value for the HM model. As for the temperature (Fig. 15), IM provides similar temperatures as HM. A zero line coincides nearly with 350 A with small positive values for lower currents (up to 4%) and small negative values for higher ones (up to −6%). Reabsorption
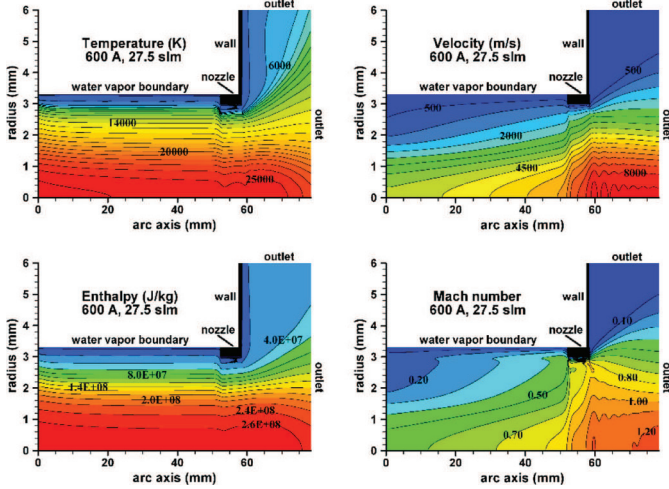
Fig. 14. Temperature, velocity, enthalpy and the Mach number contours for (600 A, 27.5 slm of argon). Results of the homogeneous mixing model (HM). Contour increments are 1000 K for temperature, 500 m s^{-1} for velocity, 2×10^7 J kg^{-1} for enthalpy, and 0.1 for the Mach number.

of radiation differs more perceptible with relative errors up +50% for 150 A with 40 slm of argon, and −20% for 600 A with 15 slm. The transition positive-negative values occurs around 400 A and continues as a curved line towards higher currents. The thicker arc fringes at lower currents are the reason for higher reabsorption of radiation in the case of IM. The effect of mixing on the plasma velocity (Fig. 16) near the exit is not so clear and simple to interpret. The maximum difference reaches ±20% – a positive value at 150 A and a negative value at 600 A for 15 slm in both cases, but for the most of the operational conditions the relative error falls below 15%. The zero line for the Mach number is near to 300 A, for lower currents the Mach numbers are very close to each other for both models, for higher currents the Mach number is higher for IM, and the highest difference reaches up to 35% for 40 slm of argon and 400 and 500 A.

4.3 Comparison with available experiments

Comparison with experiments is presented in last Figures 17–18. Experiments have been carried out with the hybrid-stabilized electric arc for currents 300–600 A with 22.5–40 slm of argon, partially overlapping with the range of parameters used in our mixing species model. Temperature and velocity profiles have been measured at the axial position of 2 mm downstream of the nozzle exit.

In experiment, the radial profiles of temperature near the nozzle exit were calculated from optical emission spectroscopy measurements. The procedure is based on the ratio of emission coefficients of hydrogen H$_\beta$ line and four argon ionic lines using calculated LTE composition of the plasma for various argon mole fractions as a function of temperature [83]. Emission coefficients of H$_\beta$ and argon lines are then obtained from the calculated molar fractions of hydrogen and argon. The temperature corresponding to

an experimental ratio of emission coefficients is then found by cubic spline interpolation on the theoretical data.

Figure 17 compares radial temperature profiles 2 mm downstream of the nozzle exit for 400, 500 and 600 A for 22.5 and 40 slm of argon. The red curves denote experiments, the blue curves the current calculation, and the dashed-black ones our former calculation using this mixing model, but with a boundary condition (14) for argon mass fraction at the argon inlet boundary, i.e. without any premixing of argon and steam plasma species. Coincidence between the experiments (red curves) and the current calculation (blue curves) seems to be very good, especially for 500 and 600 A and 40 slm. The maximum difference in the profiles is below 2 kK and they fit well in their magnitudes and shapes. For 400–500 A and 22.5 slm the peak experimental temperatures are lower, up to 2 kK for 500 A, and having higher temperatures in the arc fringes for 400 A. Since the uncertainty in measurements (error bars) is unknown the maximum difference of about 1–2 kK between the experiment and IM can be regarded as very good agreement. On the other hand, calculations with the boundary condition (14) (dashed-black curves) demonstrate higher discrepancies in most cases, except for 500 A and 22.5 slm where the both calculations nearly overlap. For 500–600 A and 40 slm the difference between the dashed-black calculations and experiments is noticeable and reaches up to 4 kK in the axial region.

In addition to temperature profiles, velocity profiles (Fig. 18) have been evaluated from the experiment. The general procedure is based on determination of the velocity near the nozzle exit from the measured temperature profile and power balance assuming LTE [84]. First, the Mach number M is obtained from the simplified energy equation integrated through the discharge volume as described in [48]. Second, the velocity profile is then derived from the measured temperature profile using the definition of the Mach number

$$u(r) = M \cdot c(r) \qquad (21)$$

where $c(r)$ is the sonic velocity profile corresponding to the experimental temperature profile $T_{exp}(r)$.

The pressure at the nozzle exit was supposed to be equal to the atmospheric pressure. As the dependence of the sonic velocity value on the pressure is weak, the possible erroneous estimation of the pressure has a negligible effect on the resulting values of velocity. For the blue curves in the plots denoted as "experiment 1" we can write equation (21) as

$$u_{exp}(r) = M_{exp} \cdot c\{T_{exp}(r), p = 1 \text{atm.}, X_A\}, \qquad (22)$$

where "exp" means the experimental value. The Mach number values evaluated from the measurements and the simplified energy balance, constant over the discharge radius are $M_{exp} = 0.58$ (400 A, 22.5 Ar slm), 0.77 (500 A, 22.5 Ar slm), 1.00 (500 A, 40 Ar slm), 1.18 (600 A, 40 Ar slm), and they indicate the existence of supersonic regime for 500 and 600 A. The profile of the sonic velocity was then interpolated from the tables of the properties used in this paper (by Murphy) for the appropriate $T_{exp}(r)$ and for the calculated argon mole fraction X_A at the axis. The
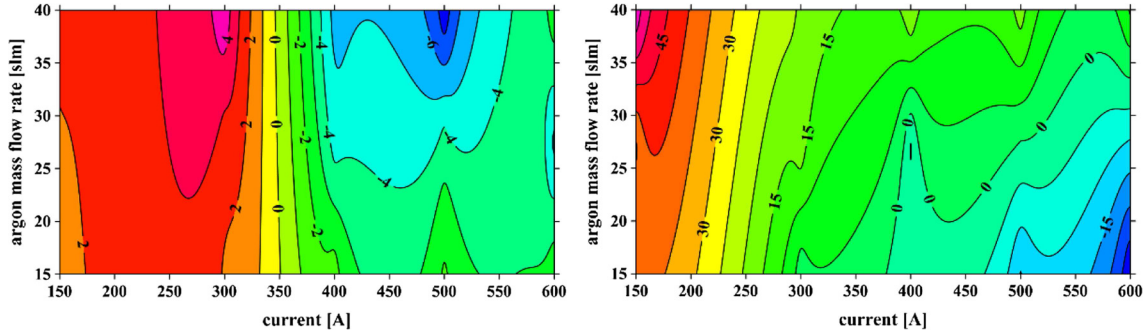
Fig. 15. Relative difference in % (see the text) between the inhomogeneous (IM) and homogeneous (HM) models. Left-temperature 2 mm downstream of the nozzle exit, right-reabsorption of radiation within the discharge, both in dependence on argon mass flow rate and current.
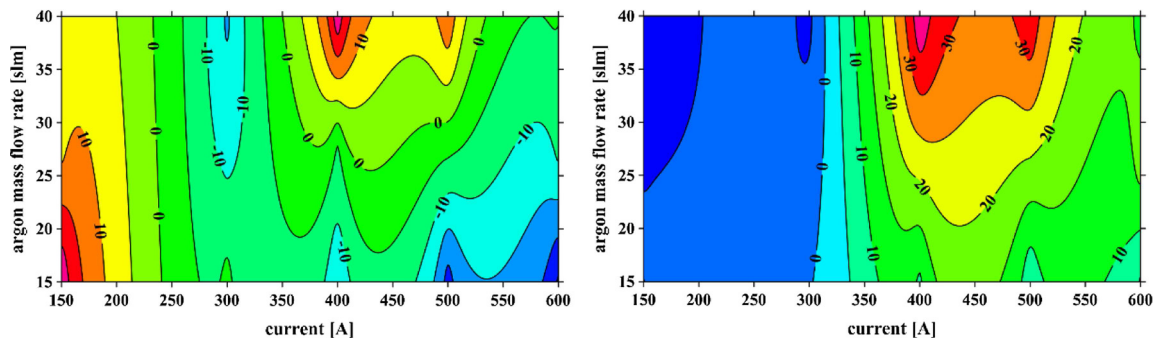

Fig. 16. The same as in Figure 15 but for velocity (left) and the Mach number (right) 2 mm downstream of the nozzle exit.

measurements of $T_{exp}(r)$ and M_{exp} were carried out 2 mm downstream of the nozzle exit.

For more exact evaluation of the velocity profiles we present here another set of profiles denoted as "experiment 2". These profiles were obtained using the so-called "integrated approach" as in [51], i.e., utilization of both experimental and numerical results: velocity profiles are determined as a product of the Mach number profiles obtained from the present numerical simulation and the sonic velocity based on the experimental temperature profiles. The modified equation (22) now reads

$$u_{int}(r) = M_{num}(r) \cdot c \{T_{exp}(r), p = 1\text{atm.}, X_A\}, \quad (23)$$

where $u_{int}(r)$ is the "integrated" velocity profile and $M_{num}(r)$ is the Mach number profile obtained from the present calculation.

Numerical simulations are displayed by the solid-black profiles. For comparison we show here the simulations employing the "original" boundary condition (14) at the argon inlet boundary (dashed-black profiles), i.e., without any premixing of species.

The results shown in Figure 18 demonstrate several facts. The difference between numerical results (solid-black) and experiments (experiment 1) is large, exceeding in some cases 3 km s^{-1}. The reason is in my opinion in the assumption of the constant Mach number over the nozzle radius in the experimental evaluation, which is the main drawback of this method, leading to underestimation of the velocity profile values. Velocity profiles obtained with the calculated profiles of the Mach number (experiment 2) provide much better comparison with nearly overlapping peak velocity values in most cases, but still larger differences in the arc fringes, caused by omitting the argon mass fraction profile over the nozzle radius in the experimental evaluation. The peak calculated velocities range from 5.5 km s^{-1} (400 A) to 9 km s^{-1} for 600 A. There is a visible double peak in the velocity profile in two cases. The existence of this double peak was also mentioned in [53] but the origin of this phenomenon remained unexplained at that time. Under more detailed investigation I found that the local plasma density can increase in the axial region under some conditions due to a stronger radial gradient of the argon mass fraction towards the axis, leading thus finally to lowering of the peak velocity. This phenomenon can occur mainly because of different atomic masses of argon ($\sim$40) and hydrogen-oxygen (up to 18) species, located mainly in the arc fringes. Velocity profiles calculated with the boundary condition (14) (calculation old), shown by dashed-black lines, give completely different maximum values from the present calculation with the condition (15). The maximum values are from 3.5 km s^{-1} for 400 A to 4.0 km s^{-1} for the highest current 600 A which does not seem as realistic values. All the profiles are double-peaked. The difference between 500 and 600 A cases with 40 slm of argon is negligible, velocity practically does not increase with current. This is an indirect numerical confirmation of some kind of premixing of plasma species in the upstream discharge region.
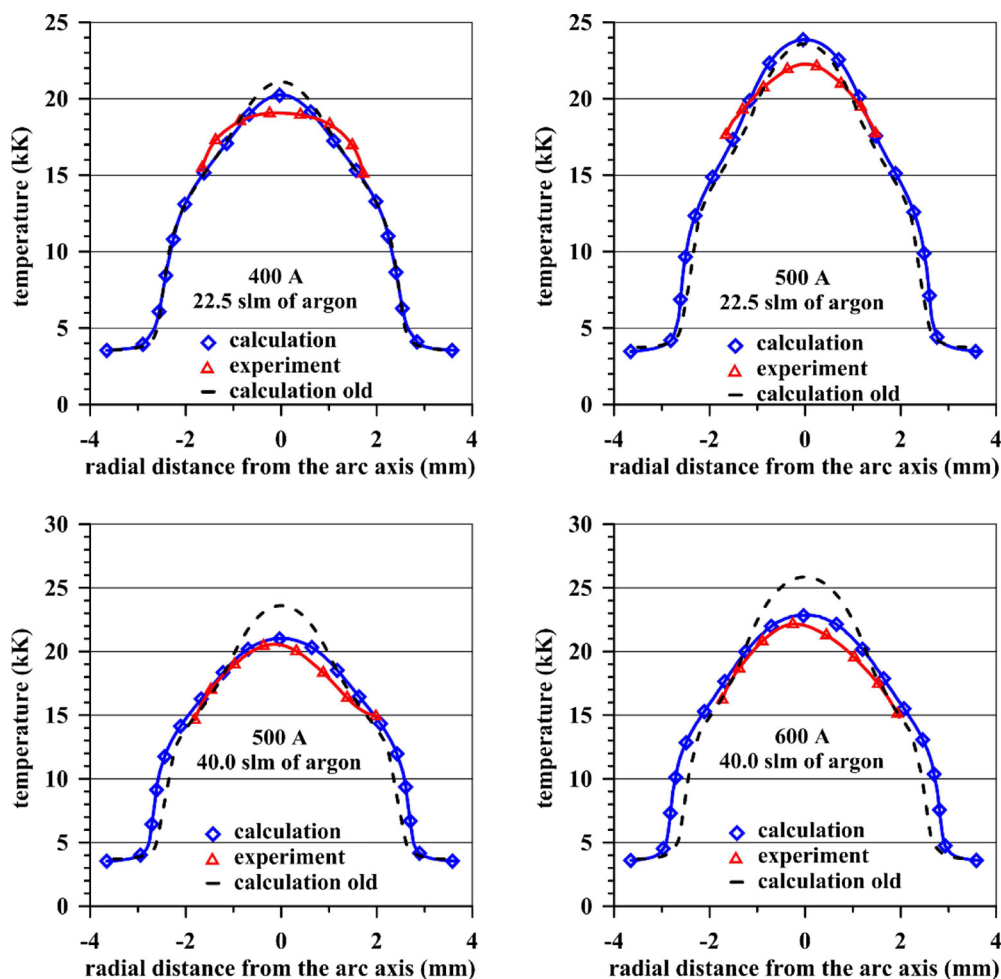
Fig. 17. Experimental and calculated radial temperature profiles 2 mm downstream of the nozzle exit for 400, 500 and 600 A, and 22.5 and 40.0 slm of argon. The present calculation is shown by a solid line, the old one (using a non-premixed boundary condition in the upstream region of the discharge) by a dashed line.

5 Conclusions

Mixing of plasma species in argon–steam arc discharge with the combined stabilization of arc by gas and water vortex has been studied in this paper. Diffusion is employed by the combined diffusion coefficients method and the diffusion processes due to gradients of mass density, temperature, pressure, and an electric field have been considered. The results of the present calculation for 150–600 A with argon mass flow rates between 15 and 40 slm can be summarized as follows:

(a) mixing of water and argon plasma species is inhomogeneous under all the studied conditions (150–600A, 15–40 slm of argon). Argon species are dominant in the central regions of the arc, water ones in the arc fringes. For higher argon mass flow rates, the amount of argon mole fraction in the central arc region increases. The maximum amount of argon mole fraction at the outlet reaches up to 0.4.

(b) The results show a principal qualitative difference between lower and higher currents for argon mole fraction, mass flux of argon species and enthalpy within the discharge:

– it was numerically clarified that at higher currents (above 300 A) argon and steam must be premixed to larger extent at the inlet region of the vortex-stabilized arc section in order to obtain a relevant agreement with available and trustworthy experimental data.

– Stronger mixing at higher currents can be explained by higher overpressure in the chamber and thicker arc column with higher temperature, causing stronger interaction of the plasma with surrounding steam.

– The interesting physical result is that premixing has a long-distance (global) impact on the plasma jet parameters near the exit nozzle (temperature, velocity, electric field strength) as well as on the overall arc performance (energy balance, influenced by temperature distribution). In contrast, the chosen form of the inlet temperature profile has only little impact on the global properties of the plasma jet, as mentioned previously [51].
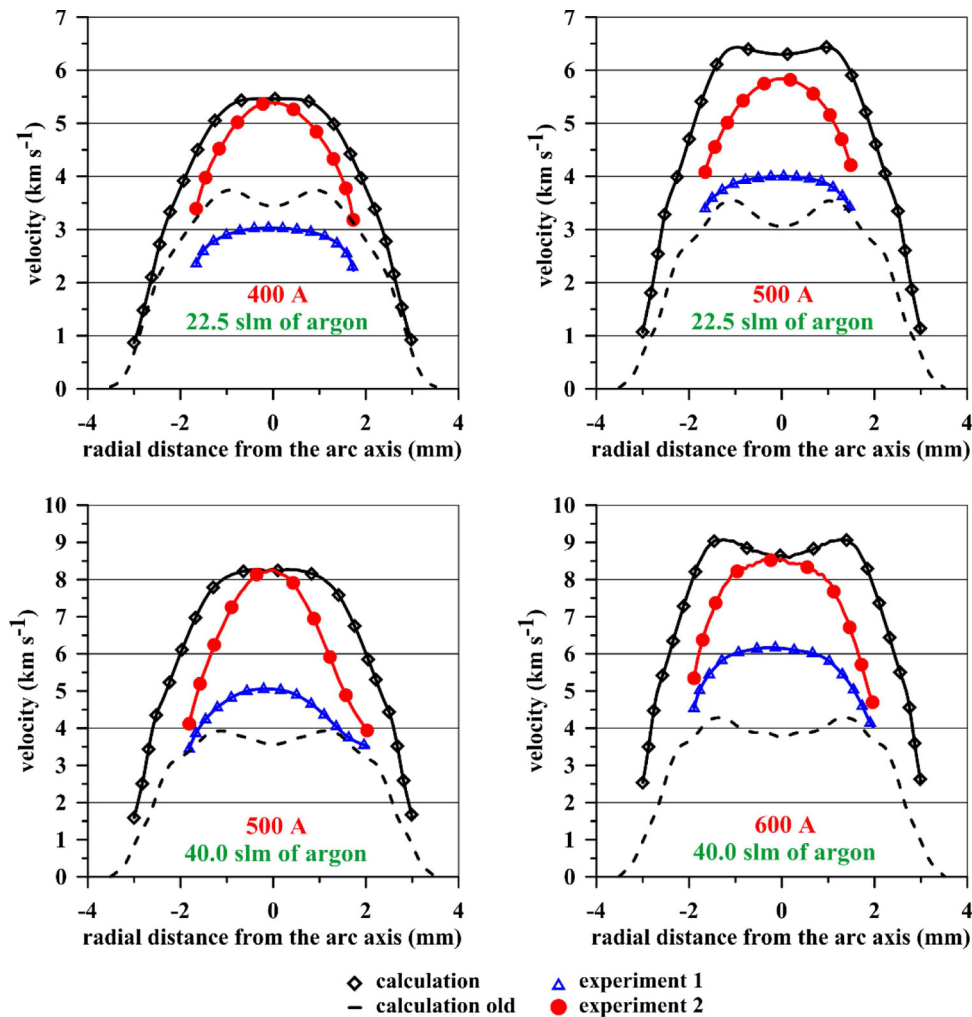
Fig. 18. The same as in Figure 17 but for the velocity profiles.

– A model function for the inlet argon mass fraction profile has been found providing the best fit between simulation and experiments for currents higher or equal to 400 A. A double-peak in the radial velocity profile under some operational conditions occurs due to a steeper radial gradient of argon species towards the discharge axis.

(c) All the combined diffusion coefficients exhibit highly nonlinear distributions of their values within the discharge, depending on temperature, pressure, and argon mass fraction in the plasma. Values of the combined diffusion coefficients are higher for temperatures below 15 kK.

(d) Reabsorption of radiation in the discharge is higher for low currents due to the thicker low-temperature arc fringes. The dependence of amount of reabsorption on argon mass fraction for a given current is insignificant.

(e) The dominant chemical species in the discharge at the exit nozzle are the atoms and ions of hydrogen, oxygen, argon, and the OH molecule.

(f) Comparison with our former calculations based on the homogeneous mixing assumption showed the following facts:

– there is a difference in temperature distribution: below 350 A the arc is slightly squeezed with higher temperatures at the axis and the arc fringes are thicker, i.e. the regions with low temperatures are wider. For higher currents the opposite is true.
– The mixing model provides higher reabsorption of radiation at low currents (below ∼350 A), and slightly lower at high currents.
– Enthalpy shows a qualitatively different distribution with maximum values shifted from the arc axis for currents higher than 400 A.
– Velocity at the outlet region does not exhibit a simple dependence, it can be higher or lower, depending on the conditions. The principle difference is appearance of a double-peak in the radial velocity profile for 500 and 600 A, but for only some argon mass flow rates. The Mach number is lower (higher) below (above) 300 A.

(g) Comparison with our former experiments was presented for the radial temperature and velocity profiles 2 mm downstream of the exit nozzle for 400–600 A. It shows very good qualitative and quantitative agreements for temperature with the maximum difference of

about 1–2 kK between the experiment and IM. Velocity profiles calculated using the combination of experimental and calculated data ("integrated approach") provide much better comparison than those obtained from the original experiment, with nearly overlapping peak velocity values (in the most cases) but still larger differences in the arc fringes. Calculations carried out under the assumption of zero premixing of species in the upstream discharge region for currents higher than 400 A provide the velocity profiles far from experimental values.

(h) Generally speaking, the results of the present simulation elucidate our better understanding of mixing and diffusion of argon-oxygen-hydrogen species in atmospheric pressure plasmas under extreme radial temperature and mass density gradients. The validity of the obtained results can be generalized and adopted to other highly radiating arc plasmas, especially to those using argon-oxygen and argon-hydrogen mixtures in a configuration with externally positioned anode when the plasma jet flows in the direction parallel to the anode surface. The obtained results are interesting from the theoretical point of view as well as for better understanding of experiments. The results can be exploited for improvement of present plasma processing technologies and for investigation of new methods of thermal plasma processing, like plasma spraying and material treatment.

Author contribution statement

Jiří Jeništa elaborated the numerical code, performed the calculations, analyzed the results and drafted the manuscript. Hidemasa Takana and Hideya Nishiyama participated in elaboration of the code, in the discussion and review of the results and provided valuable comments. Milada Bartlová and Vladimír Aubrecht calculated radiation properties of the plasma used in the simulation. Anthony B. Murphy supported this research with the plasma properties, including the combined diffusion coefficients, and provided many valuable comments about the physical model.

References

1. P. Fauchais, A. Vardelle, IEEE Trans. Plasma Sci. **25**, 1258 (1997)
2. E. Pfender, Plasma Chem. Plasma Process. **19**, 1 (1999)
3. A.B. Murphy, B. Hiraoka, J. Phys. D: Appl. Phys. **33**, 2183 (2000)
4. A.B. Murphy, Phys. Rev. E **55**, 7473 (1997)
5. J.O. Hirschfelder, C.F. Curtiss, J. Chem. Phys. **17**, 1076 (1949)
6. J.D. Ramshaw, J. Non-Equilib. Thermodyn. **15**, 295 (1990)
7. R. Taylor, R. Krishna, *Multicomponent Mass Transfer* (Wiley, New York, 1993)
8. J.D. Ramshaw, C.H. Chang, J. Non-Equilib. Thermodyn. **21**, 223 (1996)
9. J.D. Ramshaw, C.H. Chang, Plasma Chem. Plasma Process. **11**, 395 (1991)
10. A.B. Murphy, Phys. Rev. E **48**, 3594 (1993)
11. A.B. Murphy, J. Phys. D: Appl. Phys. **31**, 3383 (1998)
12. A.B. Murphy, Phys. Rev. Lett. **73**, 1797 (1994)
13. S. Ghorui, M. Vysohlid, J.V.R. Heberlein, E. Pfender, Phys. Rev. E **76**, 016404 (2007)
14. A.M. Fudolig, H. Nogami, J. Yagi, ISIJ Int. **36**, 1222 (1996)
15. V. Colombo, C. Deschenaux, E. Ghedini, M. Gherardi, C. Jaeggi, M. Leparoux, V. Mani, P. Sanibondi, Plasma Sources Sci. Technol. **21**, 045010 (2012)
16. M. Schnick, U. Fuessel, M. Hertel, M. Haessler, A. Spille-Kohoff, A.B. Murphy, J. Phys. D: Appl. Phys. **43**, 434008 (2010)
17. H-P. Li, X. Chen, Plasma Chem. Plasma Process. **22**, 27 (2002)
18. H.X. Wang, X. Chen, H-P. Li, Plasma Chem. Plasma Process. **31**, 373 (2011)
19. F. Yang, M. Rong, Y. Wu, R. Ma, A.B. Murphy, H. He, F. Bai, IEEE Trans. Plasma Sci. **39**, 2862 (2011)
20. M. Hrabovský, V. Kopecký, V. Sember, T. Kavka, O. Chumak, M. Konrád, IEEE Trans. Plasma Sci. **34**, 1566 (2006)
21. M. Hrabovský, Open Plasma Phys. J. **2**, 99 (2009)
22. Y. Ando, N. Yoshimasa, A. Kobayashi, Vacuum **110**, 190 (2014)
23. S.W. Chau, S.Y. Lub, P.J. Wang, Comput. Phys. Commun. **182**, 152 (2011)
24. S.W. Chau, C.M. Tai, S.H. Chen, IEEE Trans. Plasma Sci. **42**, 3797 (2014)
25. P. Chraska, J. Dubsky, K. Neufuss, J. Pisacka, J. Therm. Spray Technol. **6**, 320 (1997)
26. P. Ctibor, O. Roussel, A. Tricoire, J. Eur. Ceram. Soc. **23**, 2993 (2003)
27. J. Matejicek, Y. Koza, V. Weinzettl, Fusion Eng. Des. **75-79**, 395 (2005)
28. T. Chráska, K. Neufuss, J. Dubský, P. Ctibor, P. Rohan, Ceram. Int. **34**, 1229 (2008)
29. H. Ageorges, P. Ctibor, Surf. Coat. Technol. **202**, 4362 (2008)
30. J. Matejicek, T. Kavka, G. Bertolissi, P. Ctibor, M. Vilemova, R. Musalek, B. Nevrla, J. Therm. Spray Technol. **22,** 744 (2013)
31. R. Musalek, G. Bertolissi, J. Medricky, J. Kotlan, Z. Pala, N. Curry, Surf. Coat. Technol. **268**, 58 (2015)
32. P. Ctibor, J. Čížek, J. Sedláček, F. Lukáč, J. Am. Ceram. Soc. **100**, 2972 (2017)
33. G. Van Oost, M. Hrabovský, V. Kopecký, M. Konrád, M. Hlína, T. Kavka, O. Chumak, E. Beeckman, J. Verstraeten, Vacuum **80**, 1132 (2006)
34. G. Van Oost, M. Hrabovský, V. Kopecký, M. Konrád, M. Hlína, T. Kavka, Vacuum **83**, 209 (2009)

35. M. Hlína, M. Hrabovský, T. Kavka, M. Konrád, Waste Manage. **34**, 63 (2014)
36. N. Agon, M. Hrabovský, O. Chumak, M. Hlína, V. Kopecký, A. Mašláni, A. Bosmans, L. Helsen, S. Skoblja, G. Van Oost, J. Vierendeels, Waste Manage. **47**, 246 (2016)
37. M. Hrabovský, M. Hlína, V. Kopecký, A. Mašláni, O. Živný, P. Křenek, A. Serov, O. Hurba, Plasma Chem. Plasma Process. **37**, 739 (2017)
38. I. Hirka, O. Živný, M. Hrabovský, Plasma Chem. Plasma Process. **37**, 947 (2017)
39. J. Jenista, IEEE Trans. Plasma Sci. **32**, 464 (2004)
40. R.W. Liebermann, J.J. Lowke, J. Quant. Spectrosc. Radiat. Transf. **16**, 253 (1976)
41. V.G. Sevast'yanenko, J. Eng. Phys. **36**, 138 (1979)
42. J. Jeništa, H. Takana, H. Nishiyama, P. Křenek, M. Bartlová, V. Aubrecht, IEEE Trans. Plasma Sci. **39**, 2892 (2011)
43. J. Jeništa, H. Takana, H. Nishiyama, M. Bartlová, V. Aubrecht, P. Křenek, V. Sember, A. Mašláni, Comput. Phys. Commun. **182**, 1776 (2011)
44. S.B. Pope, *Turbulent Flows* (Cambridge University Press, 2000)
45. J. Jeništa, H. Takana, H. Nishiyama, M. Bartlová, V. Aubrecht, P. Křenek, J. Therm. Sci. Technol. **8**, 435 (2013)
46. J. Jeništa, H. Takana, H. Nishiyama, M. Bartlová, V. Aubrecht, P. Křenek, J. Phys.: Conf. Ser. **550**, 012016 (2014)
47. J. Jeništa, V. Kopecký, M. Hrabovský, in *Heat and Mass Transfer under Plasma Conditions*, edited by P. Fauchais et al. (Annals of the New York Academy of Sciences, 1999) Vol. 891, p. 64
48. J. Jeništa, J. Phys. D: Appl. Phys. **32**, 2763 (1999)
49. J. Jeništa, H. Takana, M. Hrabovský, H. Nishiyama, IEEE Trans. Plasma Sci. **36**, 1060 (2008)
50. J. Jeništa, H. Takana, H. Nishiyama, M. Bartlova, V. Aubrecht, M. Hrabovsky, J. High Temp. Mater. Process. **14,** 55 (2010)
51. J. Jeništa, H. Takana, H. Nishiyama, M. Bartlová, V. Aubrecht, P. Křenek, M. Hrabovský, T. Kavka, V. Sember, A. Mašláni, J. Phys. D: Appl. Phys. **44**, 435204 (2011)
52. J. Jeništa, H. Takana, H. Nishiyama, M. Bartlová, V. Aubrecht, P. Křenek, IEEE Trans. Plasma Sci. **42,** 2632 (2014)
53. J. Jeništa, H. Takana, S. Uehara, H. Nishiyama, M. Bartlová, V. Aubrecht, A.B. Murphy, J. Phys. D: Appl. Phys. **51**, 045202 (2018)
54. P. Ondáč, A. Mašláni, M. Hrabovský, J. Jeništa, Plasma Chem. Plasma Process. **38**, 637 (2018)
55. A.B. Murphy, J. Phys. D: Appl. Phys. **34**, R151 (2001)
56. V. Aubrecht, J.J. Lowke, J. Phys. D: Appl. Phys. **27**, 2066 (1994)
57. M. Bartlová, V. Aubrecht, Czech. J. Phys. **56**, B632 (2006)
58. A.B. Murphy, Sci. Rep. **4**, 1 (2014)
59. K. Cheng, X. Chen, Int. J. Heat Mass. Transfer **47**, 5139 (2004)
60. A.B. Murphy, C.J. Arundell, Plasma Chem. Plasma Process. **14**, 451 (1994)
61. J.O. Hirschfelder, C.F. Curtiss, R.B. Bird, *Molecular Theory of Gases and Liquids* (Wiley, New York, 1954)
62. S. Chapman, T.G. Cowling, in *The Mathematical Theory of Non-uniform Gases*, 3rd edn. (Cambridge University Press, 1970)
63. J.H. Ferziger, H.G. Kaper, in *Mathematical Theory of Transport Processes in Gases* (North-Holland, Amsterdam, 1972)
64. A.B. Murphy, Plasma Chem. Plasma Process. **20**, 279 (2000)
65. J.M. Baronnet, G. Debbagh-Noir, J. Lesinski, E. Meillot, in *Proceedings of the 7th International Symposium on Plasma Chemistry, Eindhoven, 1985* (1985), p. 836
66. N. Matsunaga, A. Magashima, J. Phys. Chem. **87**, 5268 (1983)
67. B. Amaee, W.B. Brown, Chem. Phys. **174**, 351 (1993)
68. J.R. Stallcop, H. Partridge, E. Levin, Phys. Rev. A **64**, 042722 (2001)
69. G. Chambaud, J.M. Launey, B. Levy, P. Millie, E. Roueff, F. Minh Tran, J. Phys. B: At. Mol. Phys. **13**, 4205 (1980)
70. G.D. Flesch, C.Y. Ng, J. Chem. Phys. **94**, 2372 (1991)
71. J.A. Fedchak, M.A. Huels, L.D. Doverspike, R.L. Champion, Phys. Rev. A **47**, 3796 (1993)
72. Y. Itikawa, At. Data Nucl. Data Tables **21**, 69 (1978)
73. P. André, L. Brunet, W. Bussière, J. Caillard, J.M. Lombard, J.P. Picard, Eur. Phys. J. Appl. Phys. **25**, 169 (2004)
74. R.A. Svehla, B.J. McBride, NASA Technical Note TN-D-7056, 1973
75. X.N. Zhang, A.B. Murphy, H-P. Li, W.D. Xia, Plasma Sources Sci. Technol. **23**, 065044 (2014)
76. J. Jeništa, J. Phys. D: Appl. Phys. **36**, 2995 (2003)
77. S. Yoon, A. Jameson, AIAA J. **26**, 1025 (1988)
78. D. Kwak, C. Kiris, J. Housman, Comput. Fluids **41**, 51 (2011)
79. P.L. Roe, J. Comput. Phys. **43**, 357 (1981)
80. B. van Leer, J. Comput. Phys **32**, 101 (1979)
81. T.J. Chung, *Computational Fluid Dynamics*, 2nd edn. (Cambridge University Press, New York, 2010)
82. J. Jeništa, J. High Temp. Mater. Process. **7**, 11 (2003)
83. P. Křenek, Plasma Chem. Plasma Process. **28**, 107 (2008)
84. T. Kavka, A. Maslani, O. Chumak, M. Hrabovský, in *Proceedings of the 5th International Conference on Flow Dynamics, Sendai, 2008*, edited by S. Maruyama (LOC of the 5th ICFD, 2008) p. OS8-11